

The Phoenix Deep Survey: spectroscopic catalog

J. Afonso^{1,2,3}, A. Georgakakis⁴, C. Almeida^{5,2}, A. M. Hopkins^{6,7}, L. E. Cram⁸, B. Mobasher^{9,10},
and M. Sullivan¹¹

ABSTRACT

The Phoenix Deep Survey is a multi-wavelength survey based on deep 1.4 GHz radio imaging, reaching well into the sub-100 μ Jy level. One of the aims of this survey is to characterize the sub-mJy radio population, exploring its nature and evolution. In this paper we present the catalog and results of the spectroscopic observations aimed at characterizing the optically “bright” ($R \lesssim 21.5$ mag) counterparts of faint radio sources. Out of 371 sources with redshift determination, 21% have absorption lines only, 11% show AGN signatures, 32% are star-forming galaxies, 34% show narrow emission lines that do not allow detailed spectral classification (due to poor signal-to-noise ratio and/or lack of diagnostic emission lines) and the remaining 2% are identified with stars. For the star-forming galaxies with a Balmer decrement measurement we find a median extinction of $A_{H\alpha} = 1.9$ mag, higher than that of optically selected samples. This is a result of the radio selection, which is not biased against dusty systems. Using the available spectroscopic information, we estimate the radio luminosity function of star-forming galaxies in two independent redshift bins at $z \approx 0.1$ and 0.3 respectively. We find direct evidence for strong luminosity evolution of these systems consistent with $L_{1.4 \text{ GHz}} \propto (1+z)^{2.7}$.

¹Universidade de Lisboa, Faculdade de Ciências, Observatório Astronómico de Lisboa, Tapada da Ajuda, 1349-018 Lisboa; jafonso@oal.ul.pt

²Centro de Astronomia e Astrofísica da Universidade de Lisboa

³Onsala Space Observatory, S-43992 Onsala, Sweden

⁴Institute of Astronomy & Astrophysics, National Observatory of Athens, I. Metaxa & B. Pavlou, Penteli, 15236, Athens, Greece

⁵Institute for Computational Cosmology, University of Durham, Durham DH1 3LE, UK

⁶Department of Physics and Astronomy, University of Pittsburgh, 3941 O’Hara Street, Pittsburgh, PA 15260, USA

⁷Hubble Fellow

⁸The Australian National University, Canberra ACT 0200 Australia

⁹Space Telescope Science Institute, 3700 San Martin Drive, Baltimore MD 21218, USA

¹⁰Also affiliated to the Space Sciences Department of the European Space Agency

¹¹Department of Astronomy and Astrophysics, University of Toronto, 60 St. George Street, Toronto, ON M5S 3H8, Canada

Subject headings: galaxies: evolution — galaxies: starburst — radio continuum: galaxies — surveys

1. Introduction

Deep radio surveys reveal, below a few milliJansky, a population of sources (the sub-mJy radio population) that is significantly different from the “classical” active galactic nucleus (AGN) powered radio galaxies typical at higher flux levels. This is clearly revealed in the normalized differential radio source counts, which shows a flattening at ~ 1 mJy that is not reproducible by evolutionary models of the mJy and Jy radio population (Danese et al. 1985, 1987; Dunlop & Peacock 1990).

Initial follow-up observations identified many of the sub-mJy sources with blue, often morphologically disturbed, galaxies (Kron, Koo, & Windhorst 1985; Windhorst et al. 1985; Thuan & Condon 1987; Windhorst, Mathis & Neuschaefer 1990). Optical spectroscopy has revealed a large fraction of galaxies with spectra indicative of star formation ($\sim 1 - 100 M_{\odot} \text{ yr}^{-1}$), similar to nearby galaxies detected by the InfraRed Astronomical Satellite (IRAS), and extending to $z \sim 1$ (Franceschini et al. 1988; Benn et al. 1993; Hammer et al. 1995; Georgakakis et al. 1999; Gruppioni, Mignoli, & Zamorani 1999; Prandoni et al. 2001). Satisfactory models of the faint radio source counts require the inclusion of an evolving population of such star-forming galaxies (Rowan-Robinson et al. 1993; Hopkins et al. 1998, 1999) in addition to the AGN population.

Interest in the sub-mJy population has increased significantly in recent years. Firstly, deep radio surveys are an efficient tool for compiling star-forming galaxy samples to $z \approx 1$. This is essential to constrain the evolution of these systems, and to estimate the global star formation rate density out to cosmologically interesting redshifts. Unlike the optical and UV, radio wavelengths are insensitive to dust obscuration. Therefore, radio selection not only provides samples that are not biased against dusty starbursts, but also does not require the large and uncertain corrections for dust extinction that have plagued optical/UV studies (e.g., Afonso et al. 2003). Secondly, there is some overlap between the still mysterious sub-millimeter galaxy population, possibly dominated by dusty star-forming galaxies at high redshifts, and very faint ($S_{1.4 \text{ GHz}} \lesssim 200 \mu\text{Jy}$) radio galaxies (Barger, Cowie, & Richards 2000; Carilli et al. 2001). The radio emission of these sub-mm sources is often the best available clue in refining the source position to allow optical identification (Blain 1999). It also provides an initial, if coarse, redshift estimate (Carilli & Yun 1999), which may be the only such estimate, since optical and near-infrared fluxes are often too faint for detection.

Despite the potential of the faint radio population for cosmological studies, there is still limited information on the nature and evolution of these systems, primarily due to incomplete redshift information and small sample sizes. Haarsma et al. (2000) combined different deep radio surveys to constrain the cosmic star formation history to $z \approx 2$. Their star formation rate density estimates are in good agreement with IR-selected samples (Rowan-Robinson et al. 1997) and much higher than those obtained from UV and optical studies. These differences most likely arise from dust induced

biases affecting the latter samples. However, the combined sample of Haarsma et al. (2000) suffers from small number statistics (total of 77 sources) and inhomogenous selection criteria due to the different frequencies, radio flux density limits and spectroscopic identification rates of the individual samples used. A systematic study of a well defined sample of radio sources at microJansky levels is necessary to securely establish the nature and evolution of these systems.

The Phoenix Deep Survey (PDS) is currently one of the largest area radio surveys reaching μJy levels, comprising over 2000 radio sources within an area of over 4.5 deg^2 to the flux density limit of about $60\mu\text{Jy}$ at 1.4 GHz (Hopkins et al. 1998, 1999, 2003a). Over the last few years, we have pursued a multiwavelength program to increase our understanding of the nature of the sub-mJy and μJy radio populations, and the evolution of star-forming galaxies (e.g., Georgakakis et al. 1999; Mobasher et al. 1999; Hopkins et al. 2000; Georgakakis et al. 2000; Afonso et al. 2001; Georgakakis et al. 2003; Afonso et al. 2003). In this paper we present the follow-up spectroscopic observations of the optically brighter ($R \lesssim 21.5$ mag) radio sources in this field, resulting in a large spectroscopic catalog of 371 redshifts that can be used for evolutionary studies. Spectroscopy of fainter optical counterparts ($R > 22$ mag) and photometric studies of yet fainter sources will be presented in forthcoming papers.

The present paper is organised as follows: in Section 2 we describe the radio and optical observations, data processing and source classification using the spectroscopic data. Section 3 presents the spectroscopic catalog, while in Section 4 the nature of the sub-mJy radio population and the obscuration of radio-selected star-forming galaxies are investigated. Section 5 explores the evolution of star-forming galaxies directly from the spectroscopic sample, through the determination of the radio luminosity function in two independent redshift bins at $z \approx 0.1$ and 0.3 . In Section 6 the conclusions are summarised.

Throughout this paper, and unless otherwise noted, we adopt a $H_0 = 70 \text{ km s}^{-1} \text{ Mpc}^{-1}$, $\Omega_M = 0.3$, and $\Omega_\Lambda = 0.7$ cosmology.

2. OBSERVATIONS

2.1. The Phoenix Deep Field radio observations

The *Phoenix Deep Survey* (PDS) includes a deep 1.4 GHz survey made using the Australia Telescope Compact Array (ATCA) covering an area of 4.56 square degrees (the Phoenix Deep Field, PDF), selected to lie in a region of low optical obscuration and devoid of bright radio sources. A noise level of $12\mu\text{Jy}$ RMS is measured in the most sensitive regions, using a resolution of $\sim 6'' \times 12''$. Source detection resulted in a catalog of 2148 sources over the whole field, with integrated fluxes ranging from $59\mu\text{Jy}$ to 114mJy . Full details of the radio observations, data reduction and source catalogs are presented in Hopkins et al. (2003a).

2.2. Optical identifications

Optical CCD imaging was carried out at the Anglo-Australian Telescope (AAT) in the R - and V -bands, as detailed in Georgakakis et al. (1999). The R -band observations cover around 70% of the PDF, while the V -band covers a smaller region. These observations are relatively shallow, being complete to $R \sim 22.5$ mag (Georgakakis et al. 1999). Deep wide field multicolour imaging ($UBVRI$) of the central part of the PDF has recently been acquired, and is presented in Sullivan et al. (2004). In the current paper, only the R -band observations of these two surveys are used, to identify optical counterparts of faint radio sources.

As described in Sullivan et al. (2004), a nearest-neighbour criterion was chosen to identify the best optical counterpart candidates. Using the R -band optical images, the $4''$ radius region surrounding each radio detection was searched for an optical counterpart. If several possibilities exist in this region, the nearest source is assumed to be the counterpart, and a flag is set to indicate the existence of multiple candidates. To give some a posteriori quantification of the likelihood of any given optical identification, the reliability (\mathcal{R}) was calculated for each identification, following the likelihood ratio method of Sutherland & Saunders (1992). Optical identifications were found for over half (1181 out of 2148) of the sources in the radio catalog of the PDS. The different optical catalogs used prevent a simple conclusion regarding the optical identification rate being drawn. However, considering only the shallow R -band observations, 46% of the radio sources are identified to $R = 22.5$ mag (the respective completeness level). When considering the deepest R -band pointing of Sullivan et al. (2004), optical identifications are found for 73% of the sources, down to $R = 24.0$ mag. These values are comparable to those found in previous work (Windhorst, Kron, & Koo 1984; Windhorst et al. 1985, 1995; Gruppioni, Mignoli, & Zamorani 1999).

2.3. Spectroscopic observations

Optical counterparts of radio sources in the PDS were observed spectroscopically in a series of observing campaigns. Initial data were obtained using multi-fibre spectroscopy at the Two Degree Field Spectrograph (2dF) at the Anglo-Australian Telescope (AAT) (Dec. 1996 and Sept. 1997) and slit spectroscopy at the ESO 3.6-m telescope (Oct. 1996). These observations were described in detail in Georgakakis et al. (1999).

Further spectroscopy was obtained at the AAT with 2dF in September 1998, August 1999, October 2000 and July 2001. The 2dF is composed of two spectrographs, each with 200 fibers having a $2''$ diameter on the sky. Sources can be targetted over a two degree diameter region. This allows the simultaneous acquisition of up to 400 low to medium resolution spectra in a wide field, and is ideal for covering large survey areas such as the PDS.

As in the initial 2dF observations, sources were separated into groups according to optical magnitude. The total exposure time varied from 1.5 h for the brightest sources to 3 h for the optically

fainter ones ($R \sim 21 - 22$ mag), each comprised of separate half-hour exposures. The September 1998 run was affected by poor weather, with only one half-hour exposure on the brightest objects being successful. Most of these sources were re-observed in later runs.

Low resolution gratings were selected, being the most appropriate for efficient redshift identification and classification. The 270R and 300B gratings were used on the 1998 run, while the 270R and 316R gratings were selected for the 1999 and 2000 runs. The final 2001 run made use of the 300B grating only. The throughput of the 270R and 316R gratings produces an effective spectral window spanning the wavelength range $5000 \lesssim \lambda \lesssim 8500 \text{ \AA}$, while that for the 300B is $4000 \lesssim \lambda \lesssim 7000 \text{ \AA}$. The spectral resolution is $\lambda/\Delta\lambda \simeq 600$ with a pixel scale of $\simeq 4.5 \text{ \AA pixel}^{-1}$. In each run, objects were distributed over the available gratings to maximise the number of allocated fibers.

2.3.1. Data processing

The spectroscopic observations were processed using the 2dF data reduction (2DFDR) package. Averaging of the reduced spectra for multiply observed individual objects was performed using the FIGARO package in the STARLINK environment.

To estimate emission line fluxes, a flux calibration was done in the following way. A relative flux calibration was performed using a response function provided by the 2dF team, calculated by estimating the 2dF efficiency in the B -, V - and R -bands and then interpolating using a second order polynomial. In order to have an estimate of the line-fluxes, the spectra were then calibrated using the measured total R -band magnitude for the observed object. This provides an “aperture correction” which is usually small since most of the galaxies observed are spatially not much bigger than the fiber. For the more extended galaxies, however, the spatial undersampling can give rise to a bias in terms of classification (the fiber will be preferentially sampling the central regions of the galaxy) and in the line luminosity. Although the number of such objects is small in this sample, and does not affect the conclusions of the statistical analysis we present, any studies of individual bright objects in the PDS will need to take this effect into consideration.

Redshifts were determined by visual inspection of the final spectra, through the identification of emission and/or absorption features. A quality flag, Q , was associated with each spectrum. A value of “A” denotes a high quality spectrum, with a firmly established redshift. A value of “B” indicates a low S/N spectrum, where a redshift was established using at least 2 spectral features. Spectra where only one spectral feature is identified, were assigned a Q value of “C”.

Line parameters (flux and equivalent widths) were determined by Gaussian fitting to identified emission and absorption features using the SPLOT package in IRAF. Several factors affect the measured line parameters. The low S/N of some of the spectra and the presence of strong atmospheric emission above 8000 \AA , not completely removed by the sky subtraction, affects the measurement of H α at $z \gtrsim 0.25$. Superposed stellar absorption, especially for the Balmer lines, will also affect

the measurements of emission in these lines. Stellar absorption at the wavelength of H β can be significant compared to typical emission line fluxes. This can be a major factor in biasing estimates of the true H β emission, and of derived quantities such as the Balmer decrement for estimating obscuration. The average H β stellar absorption is around 2 Å in star-forming galaxies (Tresse et al. 1996; Georgakakis et al. 1999; Hopkins et al. 2003b). Correction for this effect requires the knowledge of the H β absorption in each galaxy individually, something which can only be achieved with high-resolution and high S/N spectra. Consequently only the measured fluxes, including any underlying absorption, are presented here. When dealing with large samples, however, a statistical correction can be applied, as done below.

In total, quality spectra were obtained for 371 optical counterparts of radio sources. Twenty-one sources were observed both in the earlier campaigns (Georgakakis et al. 1999) and the later ones, with seventeen of these having an H α measurement. Redshift estimates agree within the measurement errors, while estimated H α luminosities agree within 30%, the expected accuracy of the flux calibration of fiber spectra. Two galaxies, however, display a much larger difference (a factor of 2) in the H α luminosity determination between the two runs. This discrepancy was traced to different fiber positions in extended ($\gtrsim 10''$), bright galaxies, an effect previously mentioned. The positions observed were offset by $\sim 2''$, (comparable to the fiber size) between different spectroscopic runs, thus sampling different physical locations of the galaxy. As mentioned above, line measurements for these objects will not be representative of the whole galaxy. In the final catalog, measurements for objects with several independent determinations (such as these ones) were averaged together.

Figure 1 shows the radio flux density and *R*-band magnitude distributions for the 371 optical counterparts of faint radio sources with quality spectra. While the radio flux density range is well sampled, only for $R \lesssim 20$ mag the optical magnitude range is significantly covered.

2.3.2. Spectral Classification

The objects with spectral line measurements were classified according to their spectra. They were divided into the following categories: (1) absorption line systems, if showing only absorption features (Balmer lines, H+K 3950 Å, 4000 Å break, MgB 5175 Å, NaD 5892 Å); (2) Seyfert 1 if presenting a broad line component in their emission line spectrum; and narrow emission line systems, either (3) Seyfert 2 or (4) star-forming, according to the properties of the emission lines detected. This separation of narrow emission line objects was done using the diagnostic emission line ratios [OIII] $\lambda\lambda 5007/\text{H}\beta$, [SII] $\lambda\lambda 6716,6731/\text{H}\alpha$, [OI] $\lambda 6300/\text{H}\alpha$ and [NII] $\lambda 6583/\text{H}\alpha$, which are believed to identify the ionizing source responsible for the emission lines, ie., young hot (OB) stars or an active galactic nucleus (AGN) (Baldwin et al. 1981; Veilleux & Osterbrock 1987; Kewley et al. 2001). As the emission line pairs are close in wavelength, these ratios are insensitive to relative effects from dust obscuration and uncertainties in the absolute flux calibration of the spectra. At redshifts $z \gtrsim 0.3$, however, the H α line moves out of the spectral window of the observations, and the ratio [OII] $\lambda 3727/\text{H}\beta$ must then be used (Rola, Terlevich & Terlevich 1997). While still sensitive to the

nature of the ionizing source, this ratio is more affected by such wavelength dependent effects.

The classification assigned to a given source was that consistent with the majority of the line ratios available for that source. To minimize incorrect classifications due to the effect of dust obscuration, higher- z sources, with only $[\text{OII}]\lambda 3727/\text{H}\beta$ and $[\text{OIII}]\lambda 5007/\text{H}\beta$ line ratios measured, were considered star-forming only if they lie in the proper region of the diagnostic diagram after a correction for an obscuration corresponding to a Balmer decrement of $\text{H}\alpha/\text{H}\beta = 6.0$ (the average value for lower- z sources in the present sample, as shown below), using the Galactic extinction curve of Cardelli, Clayton & Mathis (1989) with $R_V = 3.1$ - otherwise, the source remains unclassified.

3. The spectroscopic catalog

The Phoenix Spectroscopic Catalog was constructed using the full set of spectroscopic observations of PDS radio sources described above. For higher redshift ($z \gtrsim 0.3$) galaxies, where the $\text{H}\alpha$ line could not be measured, an $\text{H}\alpha$ luminosity was inferred using the $[\text{OII}]\lambda 3727$ flux and an assumed ratio between $[\text{OII}]\lambda 3727$ and $\text{H}\alpha$. This relation is known to be strongly luminosity and metallicity dependent (e.g., Jansen, Franx & Fabricant 2001), and this dependence has been suggested to be primarily an obscuration effect (Aragón-Salamanca et al. 2002). The relation employed here is the one found by Hopkins et al. (2003b) for radio-detected star-forming galaxies in the first data release of the Sloan Digital Sky Survey (SDSS, Abazajian et al. 2003), $F_{[\text{OII}]} = 0.23 \times F_{\text{H}\alpha}$, which appears to be suitable for the present sample, as discussed in Afonso et al. (2003).

The final spectroscopic catalog is presented in Table 1, and contains the following information:

- (1) radio source name;
- (2) $S_{1.4 \text{ GHz}}$ integrated flux density and its error;
- (3) right ascension (J2000) of the optical counterpart;
- (4) declination (J2000) of the optical counterpart;
- (5) R -band magnitude (Vega-based system) of the optical counterpart;
- (6) reliability (\mathcal{R}) of the optical identification, following Sutherland & Saunders (1992);
- (7) the measured $[\text{OII}]\lambda 3727$ equivalent width in Å;
- (8) the measured $\text{H}\beta$ equivalent width in Å;
- (9) the measured $\text{H}\alpha$ equivalent width in Å;
- (10) observed Balmer decrement ($\text{H}\alpha/\text{H}\beta$, uncorrected for any stellar absorption);
- (11) redshift z ;
- (12) spectrum quality parameter, Q ;

- (13) spectral classification;
- (14) log of H α (observed) luminosity in W;
- (15) log of 1.4 GHz luminosity in W Hz $^{-1}$.

Out of the 371 optical counterparts of faint radio sources with a redshift determination, 78 (21%) present only absorption lines in their spectra. Another 42 (11%) show signs of AGN activity (17 Seyfert 1 and 25 Seyfert 2) while 117 (32%) were classified as star-forming. For 126 (34%) sources a classification was not possible, due to the detection of too few emission lines and/or the low S/N of the lines detected. Eight sources (2%) were identified as stars. These can be either true Galactic radio stars or foreground objects coincidentally close to the radio position. Helfand et al. (1999) performed a search for radio stars using the FIRST¹ radio survey, finding an extremely low detection rate at high Galactic latitudes (less than one star with radio emission per 200 deg 2 , for $V < 10$ mag). It is likely that the present sample, much deeper at both radio and optical wavelengths, may be detecting a higher density of radio-emitting stars. The reliability (\mathcal{R}) of these identifications is in fact very high for 5 of the 8 sources, which suggests that most of these are actually Galactic radio stars. Very little is known on the luminosity function of radio stars and, hence, it is difficult to estimate what number of such objects are expected in the high galactic latitude Phoenix Deep Field (see also the discussions in Kron, Koo, & Windhorst 1985; Oort & Windhorst 1985; Benn et al. 1993). All these sources are included in our spectroscopic catalog, but candidate stars are omitted from the analysis of the extragalactic radio population in the remainder of this paper.

4. RESULTS AND DISCUSSION

4.1. Nature of the sub-mJy radio population

The present sample is used here to investigate the nature of the sub-mJy radio population for galaxies with optical counterparts. As shown in Figure 1, this will be representative of the $R \lesssim 20$ mag range. This includes a large number of sources (138) with radio flux densities below 200 μ Jy, the spectroscopic properties of which are also explored.

Figure 2 shows the radio flux density and R -band magnitude distributions for the extragalactic radio sources in the present sample according to spectral type. The corresponding redshift distribution is shown in Figure 3. It is clear that the spectroscopic survey is particularly sensitive to the low and intermediate redshift ($z \lesssim 0.5$) objects. This will be to a significant extent due to the magnitude cut-off imposed by the spectroscopy. This can be seen from Figure 4, which shows the Hubble R -band diagram for the present sample. Also shown are the predictions for M^* early- and late-type galaxies (using the values from Nakamura et al. 2003), adopting the evolutionary

¹Faint Images of the Radio Sky at Twenty-cm (Becker, White & Helfand 1995).

scenario of Pozzetti, Bruzual, & Zamorani (1996) which make use of the population synthesis code of Bruzual & Charlot (1993). Extrapolating the broad relationship followed by faint radio sources, we can see that incompleteness due to the magnitude limit of the spectroscopic survey becomes important above $z \sim 0.5$.

The increase of the star-forming galaxy population for sub-mJy fluxes (e.g., Benn et al. 1993; Georgakakis et al. 1999) is evident. While 11% of the sources with radio fluxes $S_{1.4\text{GHz}} \geq 1\text{mJy}$ show a spectrum indicative of active star formation, at sub-mJy levels this number increases to nearly 40%. Table 2 summarizes the observed behavior, from the milliJansky down to the microJansky level. The star-forming population in the present optical magnitude range appears to dominate at microJansky fluxes, while the number of absorption line and Seyfert galaxies drop steadily towards fainter radio fluxes. Unclassified objects, however, increase significantly at the faintest radio flux density levels. This can be attributed, at least partly, to fainter average optical magnitudes with decreasing radio flux density. As Figure 5 shows, the optical magnitude distribution of the μJy radio sources appears to be lacking the brighter optical counterparts seen in the $0.2\text{mJy} \leq S_{1.4\text{GHz}} < 1.0\text{mJy}$ flux density range. Consequently, the median R -band magnitude gets fainter by 0.7 magnitudes between the two radio flux density bins. Interestingly, this disappearance of bright optical counterparts for $S_{1.4\text{GHz}} < 0.2\text{mJy}$ is reflected in a corresponding lack of lower redshift objects, when sub-mJy sources with fluxes above and below 0.2 mJy are compared (Figure 5). This behavior could explain the higher fraction of spectra with lower S/N (fainter optical magnitudes) and where a classification is more difficult (sources at higher redshifts). Deeper optical spectroscopy, currently underway, is thus necessary to perform a detailed study of the faintest radio sources.

4.2. Obscuration of star-forming galaxies

The present dataset can be used to investigate the obscuration affecting radio-selected star-forming galaxies. Previous studies (Hopkins et al. 2003b; Afonso et al. 2003, the latter using a preliminary sub-sample of the present catalog) have shown that radio selection, avoiding dust-induced biases, can give quite different results to optically-selected surveys. In particular, Hopkins et al. (2003b) derives a value of $A_{H\alpha} = 1.2\text{mag}$ for optically selected star-forming galaxies in the first release of the Sloan Digital Sky Survey data (Abazajian et al. 2003), while a higher value of $A_{H\alpha} = 1.6\text{mag}$ is obtained for the subsample of galaxies with radio detection in the FIRST survey.

Figure 6 shows the distribution of Balmer decrements ($H\alpha/H\beta$) and derived emission-line obscuration values for $H\alpha$, $A_{H\alpha}$, for star-forming galaxies in the PDS, using the standard Galactic extinction curve of Cardelli, Clayton & Mathis (1989) with $R_V = 3.1$. Stellar absorption of the Balmer lines was corrected for assuming an average value of 2\AA for the equivalent width (EW) of the $H\beta$ absorption in star-forming galaxies (Tresse et al. 1996; Georgakakis et al. 1999), with a similar value (2.1\AA) being used for the $H\alpha$ line (equation (2) of Miller & Owen 2002). The corresponding distributions for the subsample of galaxies with radio detection in the FIRST survey

of Hopkins et al. (2003b) is also shown in this Figure by a solid histogram, scaled down to allow the comparison of the shapes of the distributions. A median value of $A_{H\alpha} = 1.9$ mag is found, somewhat higher than the $A_{H\alpha} = 1.6$ mag estimated by Hopkins et al. (2003b). Although the spread in $A_{H\alpha}$ is large, and it might be tempting to think that there is little significant difference in these values, the distributions look different, the present sample being more uniformly distributed to higher values of $A_{H\alpha}$. In fact, a KS test between the present sample and the radio-detected SDSS star-forming galaxies in Hopkins et al. (2003b) shows that the two are not drawn from a single parent distribution at the 99.9% confidence level. The observed difference is likely to be due to the radio selection of the PDS, unbiased against highly obscured galaxies. We note, however, that the requirement of an optical spectroscopic measurement with $H\alpha$ and $H\beta$ may still result in a bias against the most obscured star-forming galaxies. It is likely that the true average obscuration value for star-forming galaxies is higher still.

4.3. Nature of the unclassified radio population

The existence of the unclassified radio population prevents a complete quantitative analysis of the distribution of sub-mJy and μ Jy sources (for $R \lesssim 20$ mag) in star-forming and AGN systems. For all of these sources, though, at least one emission line was observed. How can their characterization be taken further?

A first approach is to study their radio luminosity. Even the most intense starbursts will not give rise to the highest radio powers observed in some AGN ($L_{1.4\text{GHz}} \gtrsim 10^{25-26} \text{ W Hz}^{-1}$), and most star-forming galaxies will display radio luminosities substantially lower. The distribution of radio luminosity according to spectroscopic classification for the present sample is presented in Figure 7. The sources with $S_{1.4\text{GHz}} < 200 \mu\text{Jy}$ are represented by a dark cross-hatched histogram. A weak bimodality exists between star-forming galaxies and absorption line systems or Seyfert galaxies. Star-forming galaxies cover the $10^{20-24.5} \text{ W Hz}^{-1}$ range, with a median value of $L_{1.4\text{GHz}} \approx 10^{22.4} \text{ W Hz}^{-1}$. Sub-mJy Seyfert and absorption line galaxies cover a wider range ($10^{20-26.5} \text{ W Hz}^{-1}$ for the former, $10^{20-25} \text{ W Hz}^{-1}$ for the latter), displaying a median value of $L_{1.4\text{GHz}} \approx 10^{23.2} \text{ W Hz}^{-1}$. The faintest ($S_{1.4\text{GHz}} < 200 \mu\text{Jy}$) radio population shows approximately the same behavior, although a lack of the highest luminosity objects is apparent. Also noteworthy is the existence of a number of absorption line and Seyfert systems with relatively low radio power ($L_{1.4\text{GHz}} < 10^{22} \text{ W Hz}^{-1}$).

With the lack of the star-forming systems above $10^{24.5} \text{ W Hz}^{-1}$, it might seem reasonable to classify otherwise unclassified systems with higher radio luminosities as AGN dominated systems. We note that this radio luminosity translates to a star formation rate of $1750 M_\odot \text{ yr}^{-1}$ (using the calibration from Bell 2003), and few galaxies are expected to have higher star formation rates. For the majority of the unclassified systems, though, the lack of a clear bimodality in the luminosity distribution between star-forming and AGN systems makes a distinction impossible. Radio luminosity alone thus seems of very limited use for classifying sources in deep radio surveys.

The radio-to-optical flux ratio can also be investigated as a possible type discriminant for the unclassified objects. Using a large sample of milliJansky radio sources classified through their mid and far-infrared IRAS fluxes, radio morphology and radio polarimetry, Machalski & Condon (1999) showed that this parameter separates between normal/star-forming galaxies and AGNs (their Figure 5). Following their procedure, we define the radio to optical flux ratio, $r_{1.4}$, as

$$r_{1.4} = \log(S_{1.4\text{GHz}}/f_R) \quad (1)$$

where f_R is the flux density at 6700 Å calculated from the measured R -band magnitude:

$$f_R = 3.0 \times 10^{6-0.4*R} (\text{mJy}). \quad (2)$$

The distribution of radio-optical flux ratio for the present sample, as a function of source type, is shown in Figure 8.

The star-forming population shows a well defined distribution, very similar to the one found by Machalski & Condon (1999). The absorption line and Seyfert galaxy populations, however, while showing a distribution with higher $r_{1.4}$, are not as distinct from the star-forming population as observed by Machalski & Condon (1999). The $r_{1.4}$ distribution for AGNs in the present sample seems to be shifted to much lower values than those sampled in the Machalski & Condon (1999) sample. For $S_{1.4\text{GHz}} < 200 \mu\text{Jy}$ this separation becomes indistinguishable, although here we are dealing with a relatively small sample.

Given the fainter radio and optical detection limits of the current survey, it is necessary to confirm that similar ranges of $r_{1.4}$ are indeed being probed in each case. The sample from Machalski & Condon (1999) uses radio sources from the NVSS² radio survey, with radio flux densities $S_{1.4\text{GHz}} > 2.5 \text{ mJy}$ and optical counterparts brighter than $R \sim 18 \text{ mag}$. For the PDS, the limits are $S_{1.4\text{GHz}} > 0.059 \text{ mJy}$ and $R \lesssim 22 \text{ mag}$. The range of $r_{1.4}$ spanned by both samples is shown in Figure 9. While there is a factor of ~ 50 separating the radio flux density limits sampled, there is an almost equivalent improvement in the optical magnitude limit for the PDS, allowing a similar range of $r_{1.4}$ to be probed. Consequently, the bimodal distribution in $r_{1.4}$ between AGNs and star-forming galaxies, if existent, should be seen in the present work. It is worth noting, however, that for $S_{1.4\text{GHz}} < 200 \mu\text{Jy}$ one would need to reach $R \sim 26 \text{ mag}$ to sample the highest values of $r_{1.4}$.

Being a flux ratio, $r_{1.4}$ is sensitive to redshift effects. However, the variation of this parameter for the same galaxy within the redshift range of interest ($z \lesssim 0.5$, both in the present sample and in Machalski & Condon 1999) is, at most, a few tenths, due to the different rest-frame emission sampled. Furthermore, the redshift range sampled by Machalski & Condon (1999) and in the present sample is similar ($z \lesssim 0.4$ for the former, $z \lesssim 0.5$ for the latter). Considering a correction

²NRAO VLA Sky Survey (Condon et al. 1998).

for the slightly higher redshift range sampled or, more directly, restricting the PDS sample to $z = 0.4$, does not change Figure 8 significantly.

The differences in the radio-optical flux ratio distributions seem instead to be due to the different classification methods employed. The classification of Machalski & Condon (1999) use radio morphology (by looking for the existence of radio lobes or jets) and polarimetry to identify AGN galaxies, which guarantees a selection of high radio luminosity AGN with large values of $r_{1.4}$, but misclassifying many low-power AGN (as indeed observed by Sadler et al. 2002). The spectroscopic-based classification for Phoenix sources, on the other hand, reveals low luminosity AGN equally well, and these show much lower values of $r_{1.4}$.

Figure 8 reveals some differences between the $r_{1.4}$ distributions for star-forming and AGN galaxies, although they are not clear enough to easily disentangle the nature of the unclassified sources in this survey. The median $r_{1.4}$ value for the unidentified sample is closer to the one found for AGNs than for star-forming systems, which could favor an AGN interpretation for the nature of the majority of these systems. There is another factor, though, that needs to be taken into account. As indicated by Barger, Cowie, & Richards (2000), there is some overlap between sub-mJy radio sources and galaxies revealed by mm and sub-mm surveys. These are thought to be dusty star-forming galaxies at higher redshifts $z \sim 1 - 3$, which would be revealed as sub-mJy and microJansky radio sources. As shown above, heavily obscured galaxies do exist in the PDS (see also Afonso et al. 2001). Radiation at optical wavelengths would be suppressed by dust, which would result in high radio-optical flux ratios, easily occupying any adopted “AGN regime”. Figure 10 shows some indication for this effect. Star-forming galaxies in the present sample are represented, with those that have a (Balmer decrement) obscuration measurement identified. Among these, the ones with the highest obscuration ($A_{H\alpha} > 3.0$ mag) show a tendency for higher $r_{1.4}$ values, as expected. Unfortunately, the number of galaxies with available Balmer decrement measurements is still too small to draw any reliable inferences. Larger surveys, such as the SDSS, would be ideal for investigating the relation between $r_{1.4}$ and obscuration values. We note that the star-forming galaxies with the highest values of $r_{1.4}$ in Figure 10 are at redshifts too high ($z \gtrsim 0.25$) for a Balmer decrement measurement with the present set of observations. These could indeed be more obscured galaxies, since there is a selection of more luminous radio systems at higher redshifts, simply due to the flux limited nature of the present survey. As seen in Afonso et al. (2003) and Hopkins et al. (2003b), more luminous radio star-forming galaxies are also expected to display, on average, a higher obscuration.

5. Evolution of star-forming galaxies

Modelling of radio source counts at sub-mJy levels requires a population of evolving star-forming galaxies (Rowan-Robinson et al. 1993; Hopkins et al. 1998). Though attempts have been made to identify this evolution directly, through spectroscopy of optical counterparts (eg Mobasher et al. 1999), the number of radio sources with spectroscopic information has been too low to

result in direct evolution detection. Adding further information from photometric redshifts and classifications has been used to provide a successful indication of the evolution present in the sub-mJy radio population (Haarsma et al. 2000).

The present sample, being more complete and homogeneous than previous investigations, allows for a direct test of evolution in the faint radio star-forming population. This is done here by calculating the radio luminosity function for star-forming galaxies in two independent redshift bins: “locally”, defined here as $z \leq 0.2$, and at higher redshifts, $0.2 < z \leq 0.5$.

5.1. Radio Luminosity Function of star-forming galaxies

To calculate the radio luminosity function for star-forming galaxies, only sources with this spectroscopic classification and radio flux densities in the range $150 \mu\text{Jy} \leq S_{1.4\text{GHz}} \leq 3 \text{mJy}$ inside the optically observed region were considered. The lower limit to radio flux prevents the faintest sources from being included in the luminosity function determination, since those sources are only detected in a small fraction of the survey area. Furthermore, at the faintest radio flux levels the unclassified sources become as abundant as the star-forming population, which could cause a significant error in the luminosity function determination. The R -band magnitudes were limited to the completeness level of the optical survey, $R \leq 22.5$ mag. Incompleteness is then present due to: (1) only a fraction of radio sources having optical identifications and (2) only a fraction of these being observed spectroscopically and resulting in a redshift determination. The simplest correction for these biases can be done by defining completeness functions $\eta_1(S_{1.4\text{GHz}})$ and $\eta_2(R)$, respectively the ratio of the number of radio sources with optical identification to the total number of radio sources and the ratio of the number of galaxies with a measured redshift to the total number of sources with optical counterparts in the sample. Figure 11 presents $\eta_1(S_{1.4\text{GHz}})$ and $\eta_2(R)$, showing the $\sim 50\%$ optical identification rate and the good spectroscopic coverage for $R \lesssim 20$ mag, where around 70% of the sources with optical identification have a redshift determination.

The radio luminosity function was thus estimated for the star-forming sample described above as

$$\Phi(L_{1.4\text{GHz}}) = \sum_{i=1}^n \frac{1}{V_{max,i}} \quad (3)$$

with an associated error of

$$\sigma^2 = \sum_{i=1}^n \left(\frac{1}{V_{max}} \right)_i^2 \quad (4)$$

with the summation over the number of galaxies in radio luminosity bins. V_{max} is calculated, for each source, by

$$V_{max} = \Omega \frac{c}{H_0} \int_{z1}^{z2} \frac{\eta_1(S_{1.4\text{GHz}}) \eta_2(R) d_L^2}{(1+z)^2 \sqrt{\Omega_M (1+z)^3 + \Omega_\Lambda}} dz \quad (5)$$

where d_L is the luminosity distance, and the integral limits are $z1 = \max(z_{radio}, z_{optical}, z_{min})$ and $z2 = \min(z'_{radio}, z'_{optical}, z_{max})$. The quantities z_{radio} and $z_{optical}$ are, respectively, the redshifts corresponding to the bright radio flux (3.0 mJy) and optical r -band magnitude ($R = 14$ mag) limits of the sample, while z'_{radio} and $z'_{optical}$ are the maximum redshifts at which the given source could still be detected (i.e., with $S_{1.4\text{GHz}} = 0.15$ mJy and $R = 22.5$ mag). The quantities z_{min} and z_{max} are, respectively, the minimum and maximum redshifts covered by the galaxies in the radio sample considered. Ω is the solid angle over which a given radio source could have been detected, given the noise level of the radio map, while $\eta_1(S_{1.4\text{GHz}})$ and $\eta_2(R)$ are the completeness functions at the radio 1.4 GHz flux density and optical R -band magnitude of that source (given in Figure 11). R -band K -corrections were estimated using model spectral energy distributions for intermediate-type spirals, while at 1.4 GHz a spectral index of $\alpha = 0.8$ ($S_{1.4\text{GHz}} \propto \nu^{-\alpha}$), typical of star-forming galaxies, was assumed.

Radio luminosity functions were estimated for “local” galaxies, with $z \leq 0.2$, and higher redshift galaxies, at $0.2 < z \leq 0.5$. Table 3 lists the estimated luminosity function values in these redshift intervals.

Figure 12 compares the derived luminosity functions with the local radio luminosity function for star-forming galaxies of Sadler et al. (2002), in its parametric fit form (solid line). While a good agreement is seen for the low redshift determination, the luminosity function for higher redshift galaxies is measurably higher. This is in agreement with the proposed evolution of the radio luminosity function (Rowan-Robinson et al. 1993; Hopkins et al. 1998; Haarsma et al. 2000). In particular, assuming a simple luminosity evolution for the Sadler et al. (2002) luminosity function in the form $L_{1.4\text{GHz}} \propto (1+z)^Q$, with $Q = 2.7 \pm 0.6$ (Hopkins 2004) seems appropriate to model the observed difference (shaded region). In terms of star formation rate this corresponds to an increase from the local value of $0.018 \text{ M}_\odot \text{ yr}^{-1} \text{ Mpc}^{-3}$ to $0.035 \text{ M}_\odot \text{ yr}^{-1} \text{ Mpc}^{-3}$ at a median redshift of 0.32 (using the calibration from Bell 2003). This is also consistent with the evolutionary rates derived in previous work (Hopkins et al. 1999; Haarsma et al. 2000; Seymour et al. 2004), but arises directly from a pure spectroscopic sample of radio selected star-forming galaxies. A good coverage of the sub-mJy radio population to an optical magnitude of $R \lesssim 21$ mag seems to be necessary to start directly detecting evolution in the faint radio star-forming galaxy population. Extending the optical magnitude range covered by the spectroscopy will result in strong constraints on the evolutionary status of the sub-mJy radio star-forming population, a work currently underway in the Phoenix Deep Survey.

6. Conclusions

A catalog of spectroscopic observations of faint radio sources in the Phoenix Deep Survey has been presented and used to investigate the nature of the sub-mJy radio sources. Down to $R \lesssim 21$ mag we find a substantial fraction of star-forming galaxies (36%), with a smaller fraction of (presumably) AGN host galaxies (27%), and a large fraction of emission line galaxies for which no classification was possible (35%). Commonly used criteria ($L_{1.4\text{GHz}}$ and radio-optical flux ratio $r_{1.4}$) have been unable to establish the nature of the unclassified population, essentially due to the sensitivity of this survey to low-power AGNs.

The 1.4 GHz luminosity function for star-forming galaxies in the present sample, estimated using the spectroscopic information directly available, shows good agreement with previous determinations of the radio luminosity function for $z \leq 0.2$. At higher redshifts ($0.2 < z \leq 0.5$), the estimated luminosity function shows an evolution over the local determination, compatible with a simple model of luminosity evolution of $L_{1.4\text{GHz}} \propto (1+z)^Q$, with $Q = 2.7 \pm 0.6$.

JA gratefully acknowledges the support from the Science and Technology Foundation (FCT, Portugal) through the fellowship BPD-5535-2001 and the research grant POCTI-FNU-43805-2001. CA acknowledges support from FCT through the research grant POCTI-FNU-43805-2001. AMH acknowledges support provided by the National Aeronautics and Space Administration (NASA) through Hubble Fellowship grant HST-HF-01140.01-A awarded by the Space Telescope Science Institute (STScI). We thank the referee, Rogier Windhorst, for insightful and constructive comments that have improved this analysis.

REFERENCES

- Abazajian, K. et al. 2003, AJ, 126, 2081
Afonso, J., Mobasher, B., Chan, B., & Cram, L. 2001, ApJ, 559, L101
Afonso, J., Hopkins, A., Mobasher, B., & Almeida, C. 2003, ApJ, 597, 269
Aragón-Salamanca, A., Alonso-Herrero, A., Gallego, J., García-Dabó, C. E., Pérez-González, P. G., Zamorano, J., Gil de Paz, A. 2002, in “Star Formation through Time” (astro-ph/0210123)
Baldwin, J. A., Phillips, M. M., & Terlevich, R. 1981, PASP, 93, 5
Barger, A. J., Cowie, L. L., & Richards, E. A. 2000, AJ, 119, 2092
Becker, R., White, R., & Helfand, D. 1995, ApJ, 450, 559
Bell, E. F. 2003, ApJ, 586, 794

- Benn, C. R., Rowan-Robinson M., McMahon, R. G., Broadhurst, T.J., & Lawrence, A. 1993, MNRAS, 263, 98
- Blain, A. W. 1999, MNRAS, 309, 955
- Bruzual A., G. & Charlot, S. 1993, ApJ, 405, 538
- Cardelli, J. A., Clayton, G. C., & Mathis, J. S. 1989, ApJ, 345, 245
- Carilli, C. L. et al. 2001, ApJ, 555, 625
- Carilli, C. L., Yun, M. S. 1999, ApJ, 513, L13
- Condon, J. J., Cotton, W. D., Greisen, E. W., Yin, Q. F., Perley, R. A., Taylor, G. B., & Broderick, J. J. 1998, AJ, 115, 1693
- Danese, L., Franceschini, A., & de Zotti, G. 1985, A&A, 143, 277
- Danese, L., Franceschini, A., Toffolatti, L., & De Zotti, G. 1987, ApJ, 318, L15
- Dunlop, J. S., & Peacock, J. A. 1990, MNRAS, 247, 19
- Franceschini, A., Danese, L., de Zotti, G., & Xu, C. 1988, MNRAS, 233, 175
- Georgakakis, A., Mobasher, B., Cram, L., Hopkins, A., Lidman, C., & Rowan-Robinson, M. 1999, MNRAS, 306, 708
- Georgakakis, A., Mobasher, B., Cram, L., Hopkins, A., & Rowan-Robinson, M. 2000, A&AS, 141, 89
- Georgakakis, A., Hopkins, A. M., Sullivan, M., Afonso, J., Georgantopoulos, I., Mobasher, B., & Cram, L. E. 2003, MNRAS, 345, 939
- Gruppioni, C., Mignoli, M., & Zamorani, G. 1999, MNRAS, 304, 199
- Haarsma, D. B., Partridge, R. B., Windhorst, R. A., & Richards, E. A. 2000, ApJ, 544, 641
- Hammer, F., Crampton, D., Lilly, S., Le Fèvre, O., & Kenet, T. 1995, MNRAS, 276, 1085
- Helfand, D., Schnee, S., Becker, R., White, R., & McMahon, R. 1999, AJ, 117, 1568
- Hopkins, A. M., Mobasher, B., Cram, L., & Rowan-Robinson, M. 1998, MNRAS, 296, 839
- Hopkins, A., Afonso, J., Cram, L., & Mobasher, B. 1999, ApJ, 519, L59
- Hopkins, A. M., Georgakakis, A., Cram, L., Afonso, J., & Mobasher, B. 2000, ApJS, 128, 469
- Hopkins, A. M., Afonso, J., Chan, B., Cram., L. E., Georgakakis, A., & Mobasher, B. 2003a, AJ, 125, 465

- Hopkins, A. M., et al. 2003b, ApJ, 599, 971
- Hopkins, A. M. 2004, ApJ, 615, 209
- Jansen, R. A., Franx, M., & Fabricant, D. 2001, ApJ, 551, 825
- Kewley, L. J., Dopita, M. A., Sutherland, R. S., Heisler, C. A., & Trevena, J. 2001, ApJ, 556, 121
- Kron, R. G., Koo, D. C., & Windhorst, R. A. 1985, A&A, 146, 38
- Machalski, J., & Condon, J. J. 1999, ApJS, 123, 41
- Miller, N. A. & Owen, F. N. 2002, AJ, 124, 2453
- Mobasher, B., Cram, L., Georgakakis, A., & Hopkins, A. 1999, MNRAS, 308, 45
- Nakamura, O., Fukugita, M., Yasuda, N., Loveday, J., Brinkmann, J., Schneider, D. P., Shimasaku, K., & SubbaRao, M. 2003, AJ, 125, 1682
- Oort, M. J. A., & Windhorst, R. A. 1985, A&A, 145, 405
- Pozzetti, L., Bruzual A., G., & Zamorani, G. 1996, MNRAS, 281, 953
- Prandoni, I., Gregorini, L., Parma, P., de Ruiter, H. R., Vettolani, G., Zanichelli, A., Wieringa, M. H., & Ekers, R. D. 2001, A&A, 369, 787
- Rola, C. S., Terlevich, E., & Terlevich, R. J. 1997, MNRAS, 289, 419
- Rowan-Robinson M., Benn, C.R., Lawrence, A., McMahon, R.G., & Broadhurst, T.J. 1993, MNRAS, 263, 123
- Rowan-Robinson, M., Mann, R. G., Oliver, S. J., et al. 1997, MNRAS, 289, 490
- Sadler, E. M., Jackson, C. A., Cannon, R. D., et al. 2002, MNRAS, 329, 227
- Seymour, N., McHardy, I. M., & Gunn, K. F. 2004, MNRAS, 352, 131
- Sullivan, M., Hopkins, A. M., Afonso, J., Georgakakis, A., Almeida, C., Chan, B., Cram, L., Mobasher, B., & Almeida, C. 2004, ApJS, 155, 1
- Sutherland, W. & Saunders, W. 1992, MNRAS, 259, 413
- Thuan, T.X.,& Condon, J.J. 1987, ApJ, 322, L9
- Tresse, L., Rola, C., Hammer, F., Stasinska, G., Le Fevre, O., Lilly, S. J., & Crampton, D. 1996, MNRAS, 281, 847
- Veilleux, S., & Osterbrock, D. E. 1987, ApJS, 63, 295
- Windhorst, R. A., Kron, R. G., & Koo, D. C. 1984, A&AS, 58, 39

Windhorst, R.A., Miley, G.K., Owen, F.N., Kron, R.G., & Koo, D.C. 1985, ApJ, 289, 494

Windhorst, R., Mathis, D., & Neuschafer, L. 1990, in Kron R. G., ed., ASP Conf. Ser. Vol. 10, Evolution of the Universe of galaxies. Astron. Soc. Pac., San Francisco, p. 389

Windhorst, R. A., Fomalont, E. B., Kellermann, K. I., Partridge, R. B., Richards, E., Franklin, B. E., Pascarella, S. M., & Griffiths, R. E. 1995, Nature, 375, 471

Table 1. The PDS spectroscopic catalog

Radio source	S _{1.4 GHz} (mJy)	α (J2000)	δ (J2000)	R (mag)	\mathcal{R}	EW _{[OII]λ3727} (Å)	EW _{Hβ} (Å)	EW _{Hα} (Å)	(H α /H β) _{obs}	z	Q	Class	log L _{Hα} (W)	log L _{1.4 GHz} (W Hz $^{-1}$)
PDFJ010826.6-454227	0.524 ± 0.040	01 08 26.69	-45 42 27.0	19.15	0.99	26	0.428	C	uncl	34.78	23.51
PDFJ010830.6-454801	0.164 ± 0.038	01 08 30.63	-45 48 01.3	19.38	0.45	50	11	0.437	B	sf	34.96	23.03
PDFJ010830.7-460347	0.351 ± 0.056	01 08 30.67	-46 03 47.6	19.31	0.99	0.271	C	uncl	...	22.88
PDFJ010833.2-454543	0.288 ± 0.050	01 08 33.07	-45 45 44.3	19.98	0.99	22	0.570	C	uncl	35.18	23.54
PDFJ010834.5-455802	0.397 ± 0.048	01 08 34.44	-45 58 01.4	16.44	0.99	...	-4	0.133	B	abs	...	22.26
PDFJ010836.2-454451	0.184 ± 0.046	01 08 36.14	-45 44 51.0	15.88	0.98	0.089	B	abs	...	21.55
PDFJ010836.9-460307	0.468 ± 0.046	01 08 36.85	-46 03 07.3	18.59	0.99	125	62	190	4.65	0.285	A	sf	35.86	23.06
PDFJ010837.1-454822	0.291 ± 0.054	01 08 37.13	-45 48 22.1	15.85	0.99	...	2	26	7.52	0.027	A	sf	33.61	20.68
PDFJ010839.2-455656	0.202 ± 0.038	01 08 39.21	-45 56 55.8	17.16	0.99	25	...	0.133	A	sf	34.56	21.96
PDFJ010846.6-455502	0.475 ± 0.034	01 08 46.52	-45 55 02.5	17.71	0.99	10	2	25	28.17	0.195	A	sf	34.97	22.69
PDFJ010853.9-455838	0.951 ± 0.051	01 08 53.88	-45 58 39.6	18.11	0.99	0.233	A	abs	...	23.17
PDFJ010901.8-455953	0.236 ± 0.039	01 09 01.82	-45 59 52.2	17.45	0.99	...	8	46	10.59	0.076	A	sf	34.39	21.52
PDFJ010907.4-455056	0.179 ± 0.066	01 09 07.04	-45 50 56.3	18.69	0.37	10	3	8	5.38	0.257	B	uncl	34.22	22.54
PDFJ010907.5-454141	0.261 ± 0.041	01 09 07.59	-45 41 43.1	19.98	0.58	...	15	0.297	C	uncl	...	22.84
PDFJ010911.5-455838	0.241 ± 0.040	01 09 11.48	-45 58 39.4	18.79	0.99	34	11	0.298	A	sf	34.48	22.81
PDFJ010911.7-462008	0.175 ± 0.038	01 09 11.68	-46 02 08.0	17.55	0.99	...	1	23	...	0.090	A	sf	33.90	21.54
PDFJ010913.3-453416	2.515 ± 0.044	01 09 13.25	-45 34 16.3	17.86	0.99	24	...	23	...	0.147	A	Sey2	34.15	23.15
PDFJ010913.5-455323	4.266 ± 0.053	01 09 13.45	-45 53 23.1	19.55	0.99	6	0.530	A	uncl	34.94	24.64
PDFJ010926.9-452121	0.339 ± 0.046	01 09 26.90	-45 21 20.9	17.52	1.00	...	2	18	14.67	0.172	A	Sey2	34.74	22.43
PDFJ010930.7-460308	0.105 ± 0.034	01 09 30.62	-46 03 08.3	19.22	0.99	0.412	B	uncl	...	22.77
PDFJ010932.4-453232	0.124 ± 0.038	01 09 32.34	-45 32 33.0	18.72	0.99	11	...	20	...	0.300	B	uncl	34.96	22.53
PDFJ010933.3-454824	0.108 ± 0.028	01 09 33.28	-45 48 23.7	18.64	0.99	28	7	44	9.62	0.133	A	uncl	34.24	21.70
PDFJ010933.7-453811	0.193 ± 0.079	01 09 33.59	-45 38 09.7	18.09	0.97	15	...	0.075	A	uncl	33.55	21.42
PDFJ010933.7-453114	1.100 ± 0.061	01 09 33.72	-45 31 14.8	20.24	0.99	0.608	B	abs	...	24.19
PDFJ010936.6-453905	0.257 ± 0.070	01 09 36.64	-45 39 03.6	18.13	0.97	0.372	B	abs	...	23.06
PDFJ010937.8-455352	0.095 ± 0.028	01 09 37.75	-45 53 51.2	13.91	0.98	-1	...	0.022	A	abs	...	20.03
PDFJ010942.7-454532	0.184 ± 0.075	01 09 42.69	-45 45 36.6	19.32	0.01	0.301	B	uncl	...	22.71
PDFJ010943.6-460138	0.083 ± 0.028	01 09 43.66	-46 01 36.5	17.31	0.97	...	4	23	11.46	0.120	A	sf	34.50	21.49
PDFJ010944.0-453844	0.169 ± 0.054	01 09 43.91	-45 38 45.4	19.18	0.97	45	16	125	5.54	0.248	A	uncl	34.84	22.48
PDFJ010946.5-455001	1.883 ± 0.065	01 09 46.35	-45 50 02.3	19.96	0.92	0.545	C	abs	...	24.31
PDFJ010946.6-454657	0.888 ± 0.034	01 09 46.65	-45 46 57.2	14.47	1.00	...	2	10	11.95	0.020	A	Sey2	33.59	20.89
PDFJ010948.0-455125	0.358 ± 0.038	01 09 47.94	-45 51 24.9	14.96	1.00	10	...	0.020	A	sf	33.35	20.52
PDFJ010949.1-454031	1.539 ± 0.049	01 09 49.12	-45 40 31.1	20.76	0.99	14	0.548	C	uncl	34.73	24.23
PDFJ010950.0-454628	0.177 ± 0.028	01 09 49.96	-45 46 28.6	18.43	0.99	15	3	0.300	A	uncl	35.12	22.69
PDFJ010950.5-456116	0.138 ± 0.047	01 09 50.37	-46 01 15.4	19.40	0.98	35	0.550	C	uncl	35.42	23.18
PDFJ010951.8-455004	0.231 ± 0.040	01 09 51.71	-45 50 04.0	21.36	0.99	44	0.530	C	uncl	35.00	23.37
PDFJ010952.7-453034	0.249 ± 0.056	01 09 52.61	-45 30 35.7	18.80	0.99	21	...	0.242	A	uncl	34.59	22.62
PDFJ010954.4-460554	0.264 ± 0.082	01 09 54.59	-46 05 52.2	14.31	0.20	...	4	0.024	C	uncl	33.70	20.53
PDFJ010956.5-455900	0.112 ± 0.034	01 09 56.47	-45 59 00.5	18.75	0.99	...	13	0.253	C	uncl	34.34	22.32
PDFJ010957.5-453458	0.347 ± 0.048	01 09 57.51	-45 34 57.4	19.19	0.98	75	...	21	...	0.242	A	uncl	34.12	22.77
PDFJ011001.4-460818	0.219 ± 0.034	01 10 01.38	-46 08 18.5	19.08	0.99	3.056	B	Sey1	...	25.13
PDFJ011006.2-452151	0.201 ± 0.036	01 10 06.22	-45 21 52.0	20.39	0.99	5	0.542	A	abs	34.51	23.33
PDFJ011008.8-453020	0.233 ± 0.040	01 10 08.85	-45 30 21.1	19.98	0.99	0.357	C	abs	...	22.98
PDFJ011009.7-453100	3.283 ± 0.064	01 10 09.70	-45 31 00.2	18.96	0.99	0.372	A	abs	...	24.17
PDFJ011011.5-451551	0.097 ± 0.040	01 10 11.45	-45 15 51.5	19.71	0.99	18	56	0.543	A	sf	34.93	23.02
PDFJ011011.4-452740	0.209 ± 0.081	01 10 11.42	-45 27 42.5	16.92	0.99	...	17	51	3.43	0.046	A	sf	34.03	21.02
PDFJ011013.9-452246	0.511 ± 0.043	01 10 13.89	-45 22 46.8	19.53	0.99	43	15	0.543	A	sf	35.50	23.74
PDFJ011014.4-461507	13.538 ± 0.156	01 10 14.55	-46 15 06.5	14.89	0.90	0.000	-	star
PDFJ011015.6-453526	0.129 ± 0.038	01 10 15.49	-45 35 26.6	18.01	0.99	53	3	20	13.74	0.189	A	Sey2	34.63	22.10
PDFJ011015.6-452515	0.169 ± 0.030	01 10 15.63	-45 25 15.7	21.40	0.99	134	50	0.420	A	uncl	34.87	23.00

Table 1—Continued

Radio source	$S_{1.4 \text{ GHz}}$ (mJy)	α (J2000)	δ (J2000)	R (mag)	\mathcal{R}	$\text{EW}_{\text{[OII]}\lambda 3727}$ (Å)	$\text{EW}_{\text{H}\beta}$ (Å)	$\text{EW}_{\text{H}\alpha}$ (Å)	$(\text{H}\alpha/\text{H}\beta)_{\text{obs}}$	z	Q	Class	$\log L_{\text{H}\alpha}$ (W)	$\log L_{1.4 \text{ GHz}}$ (W Hz $^{-1}$)
PDFJ011016.3-454732	0.158 ± 0.048	01 10 16.17	-45 47 32.5	19.76	0.85	37	13	0.373	A	sf	35.16	22.85
PDFJ011018.2-455557	0.073 ± 0.030	01 10 17.98	-45 55 58.9	15.16	0.95	...	1	...	0.029	A	uncl	32.99	20.14	
PDFJ011018.1-454905	0.176 ± 0.036	01 10 18.10	-45 49 05.7	19.21	0.93	37	17	...	0.258	A	sf	35.02	22.54	
PDFJ011019.0-453328	0.080 ± 0.034	01 10 19.17	-45 33 28.2	18.67	0.99	13	...	0.236	A	uncl	34.41	22.11
PDFJ011019.6-453857	0.119 ± 0.049	01 10 19.52	-45 38 58.0	18.17	0.99	11	1	...	0.233	B	sf	34.12	22.27	
PDFJ011023.4-450338	1.532 ± 0.075	01 10 23.39	-45 03 38.3	19.79	0.99	30	0.356	B	uncl	34.37	23.79	
PDFJ011024.3-451455	0.301 ± 0.040	01 10 24.34	-45 14 55.4	19.76	0.99	34	5	...	0.417	A	Sey2	34.63	23.24	
PDFJ011025.3-452355	0.147 ± 0.050	01 10 25.11	-45 23 54.9	19.19	0.98	0.000	-	star	
PDFJ011027.7-460427	0.161 ± 0.030	01 10 27.68	-46 04 27.1	13.52	1.00	-1	...	0.022	A	abs	...	20.26
PDFJ011027.8-452255	0.786 ± 0.042	01 10 27.77	-45 22 55.7	17.74	1.00	0.234	A	abs	...	23.09	
PDFJ011028.6-452437	0.272 ± 0.037	01 10 28.51	-45 24 38.8	19.82	0.99	...	18	...	0.466	C	uncl	...	23.31	
PDFJ011029.4-461027	4.201 ± 0.092	01 10 29.40	-46 10 27.8	14.30	1.00	...	3	35	13.40	0.023	A	sf	34.34	21.72
PDFJ011029.8-454858	0.358 ± 0.036	01 10 29.73	-45 48 58.4	19.66	0.99	103	0.482	A	uncl	35.90	23.46	
PDFJ011030.2-453114	0.971 ± 0.035	01 10 30.18	-45 31 13.8	17.08	1.00	0.000	-	star	
PDFJ011030.9-460507	0.098 ± 0.030	01 10 30.80	-46 05 07.1	17.54	1.00	...	1	18	22.33	0.121	A	sf	34.45	21.56
PDFJ011032.4-454248	0.235 ± 0.028	01 10 32.36	-45 42 48.8	18.31	0.99	18	2	...	0.289	A	sf	34.46	22.77	
PDFJ011032.5-454004	0.454 ± 0.028	01 10 32.51	-45 40 04.5	19.81	0.99	...	1	60	24.20	0.412	A	Sey2	34.59	23.41
PDFJ011032.6-455405	2.107 ± 0.053	01 10 32.53	-45 54 04.8	17.0	0.99	0.255	A	abs	...	23.60	
PDFJ011033.3-454957	0.692 ± 0.085	01 10 33.33	-44 59 58.1	20.92	0.99	0.571	C	abs	...	23.92	
PDFJ011033.7-454021	0.219 ± 0.028	01 10 33.66	-45 40 21.3	18.96	0.99	77	3	...	0.410	A	uncl	35.94	23.09	
PDFJ011034.0-450755	0.220 ± 0.078	01 10 33.82	-45 07 55.1	16.88	0.98	4	...	0.124	A	uncl	33.93	21.93
PDFJ011036.4-453557	0.068 ± 0.028	01 10 36.34	-45 35 56.8	18.90	0.99	-3	...	0.071	B	abs	...	20.91
PDFJ011038.2-453819	0.163 ± 0.028	01 10 38.19	-45 38 19.3	17.41	1.00	7	3	40	8.77	0.189	A	sf	34.95	22.20
PDFJ011043.2-461050	0.203 ± 0.043	01 10 43.22	-46 10 49.5	17.86	0.99	12	...	9	...	0.229	B	uncl	34.64	22.48
PDFJ011046.6-454141	0.373 ± 0.042	01 10 46.64	-45 41 41.4	16.45	1.00	...	1	15	11.18	0.120	A	sf	34.57	22.13
PDFJ011047.8-454638	0.169 ± 0.030	01 10 47.77	-45 46 37.7	19.75	0.99	0.263	C	abs	...	22.54	
PDFJ011048.0-460133	0.074 ± 0.028	01 10 47.96	-46 01 34.1	19.01	0.99	13	...	57	...	0.298	A	uncl	35.14	22.30
PDFJ011048.4-454713	0.147 ± 0.041	01 10 48.26	-45 47 12.5	19.32	0.98	25	9	...	0.330	A	sf	34.40	22.70	
PDFJ011050.1-455037	0.074 ± 0.028	01 10 50.03	-45 50 37.0	20.82	0.99	0.406	C	uncl	...	22.61	
PDFJ011051.5-460225	0.080 ± 0.028	01 10 51.46	-46 02 27.0	19.69	0.98	60	0.570	B	uncl	35.42	22.98	
PDFJ011052.1-454338	0.080 ± 0.026	01 10 52.01	-45 43 40.2	19.73	0.98	21	4	...	0.373	A	sf	34.87	22.56	
PDFJ011052.2-453353	0.346 ± 0.037	01 10 52.16	-45 33 54.3	18.61	0.99	2	3	40	6.88	0.122	A	sf	33.99	22.12
PDFJ011053.2-460701	7.646 ± 0.086	01 10 53.15	-46 07 00.9	15.98	1.00	0.102	A	abs	...	23.30	
PDFJ011055.0-450637	0.467 ± 0.078	01 10 55.02	-45 06 37.4	19.20	0.96	0.377	C	abs	...	23.33	
PDFJ011055.8-453919	0.243 ± 0.042	01 10 55.79	-45 39 19.8	15.83	1.00	...	3	36	8.24	0.024	A	sf	33.69	20.49
PDFJ011056.3-460944	0.209 ± 0.034	01 10 56.34	-46 09 44.3	19.61	0.99	32	0.604	C	uncl	35.62	23.46	
PDFJ011057.1-455211	0.797 ± 0.031	01 10 57.14	-45 52 11.4	20.84	1.00	0.693	C	abs	...	24.18	
PDFJ011057.2-454126	0.067 ± 0.026	01 10 57.09	-45 41 24.4	20.13	0.95	125	0.567	C	uncl	36.08	22.90	
PDFJ011100.7-453156	0.071 ± 0.028	01 11 00.69	-45 31 56.7	19.31	0.99	0.229	C	uncl	...	22.02	
PDFJ011101.2-454854	0.064 ± 0.028	01 11 01.16	-45 48 54.1	20.86	0.99	0.285	C	uncl	...	22.19	
PDFJ011101.8-454157	0.064 ± 0.026	01 11 01.70	-45 41 57.4	19.05	0.99	30	4	...	0.283	A	sf	35.11	22.19	
PDFJ011102.8-462743	0.455 ± 0.077	01 11 02.69	-46 27 43.1	19.98	0.99	0.574	B	abs	...	23.75	
PDFJ011105.3-453850	0.076 ± 0.026	01 11 05.26	-45 38 49.4	21.07	0.92	19	0.538	A	uncl	34.71	22.90	
PDFJ011106.1-454918	0.239 ± 0.028	01 11 06.04	-45 49 18.9	17.77	1.00	21	8	80	5.54	0.126	A	sf	34.65	21.99
PDFJ011108.8-453621	0.153 ± 0.038	01 11 08.80	-45 36 22.4	17.25	0.99	...	1	46	11.33	0.090	A	sf	34.32	21.48
PDFJ011110.1-461010	0.152 ± 0.046	01 11 10.04	-46 10 11.4	18.20	0.99	0.231	A	abs	...	22.37	
PDFJ011112.7-455112	0.104 ± 0.028	01 11 12.63	-45 51 13.0	20.78	0.99	17	10	...	0.551	A	sf	34.72	23.06	
PDFJ011113.5-455641	0.086 ± 0.034	01 11 13.43	-45 56 42.6	18.66	0.98	22	...	0.151	A	uncl	34.15	21.71
PDFJ011113.6-460059	0.157 ± 0.034	01 11 13.51	-46 00 59.8	17.45	0.99	11	...	0.119	A	uncl	34.22	21.75
PDFJ011113.9-460824	0.128 ± 0.042	01 11 13.82	-46 08 26.3	19.05	0.99	18	4	8	5.42	0.242	B	sf	34.37	22.33

Table 1—Continued

Radio source	S _{1.4 GHz} (mJy)	α (J2000)	δ (J2000)	R (mag)	\mathcal{R}	EW _{[OII]λ3727} (Å)	EW _{Hβ} (Å)	EW _{Hα} (Å)	(H α /H β) _{obs}	z	Q	Class	log $L_{H\alpha}$ (W)	log $L_{1.4 \text{ GHz}}$ (W Hz $^{-1}$)
PDFJ011115.0-453213	0.164 ± 0.032	01 11 15.01	-45 32 14.1	18.81	0.99	0.301	A	abs	...	22.66
PDFJ011115.5-453204	0.322 ± 0.109	01 11 15.70	-45 32 04.2	19.21	0.93	8	0.370	B	uncl	34.02	23.15
PDFJ011116.0-454342	0.191 ± 0.038	01 11 15.84	-45 43 42.3	20.80	0.90	0.695	C	abs	...	23.56
PDFJ011115.8-460937	2.865 ± 0.070	01 11 15.98	-46 09 38.1	19.98	0.48	1.058	C	Sey1	...	25.17
PDFJ011118.4-454630	0.068 ± 0.028	01 11 18.31	-45 46 28.7	18.71	0.98	4	...	18	...	0.234	B	uncl	34.44	22.03
PDFJ011119.1-455051	0.094 ± 0.037	01 11 19.05	-45 50 52.1	19.29	0.99	22	13	35	7.32	0.370	B	sf	34.96	22.62
PDFJ011119.1-455554	4.730 ± 0.168	01 11 19.22	-45 55 56.0	14.39	0.99	...	-3	0.022	A	abs	...	21.71
PDFJ011120.6-461914	0.168 ± 0.042	01 11 20.56	-46 19 14.0	20.82	0.99	...	9	0.431	B	sf	...	23.02
PDFJ011121.3-454430	0.111 ± 0.044	01 11 21.22	-45 44 30.6	19.80	0.99	30	4	...	15.67	0.301	A	sf	34.82	22.49
PDFJ011123.0-452214	0.127 ± 0.042	01 11 22.84	-45 22 13.8	20.27	0.98	68	0.377	C	uncl	34.56	22.77
PDFJ011123.7-454343	0.177 ± 0.043	01 11 23.71	-45 43 43.5	20.01	1.00	50	9	...	11.75	0.332	A	Sey2	34.76	22.78
PDFJ011124.8-452912	0.285 ± 0.067	01 11 25.11	-45 29 13.1	19.23	0.27	30	0.330	C	uncl	34.17	22.99
PDFJ011125.7-453729	0.101 ± 0.028	01 11 25.64	-45 37 29.6	20.12	0.98	47	0.297	C	uncl	34.28	22.43
PDFJ011126.3-453814	0.327 ± 0.028	01 11 26.25	-45 38 14.9	17.49	1.00	24	...	0.196	B	uncl	34.78	22.54
PDFJ011126.2-453017	0.170 ± 0.064	01 11 26.36	-45 30 17.2	19.85	0.96	7	0.422	B	uncl	34.52	23.01
PDFJ011126.8-455317	0.174 ± 0.038	01 11 26.79	-45 53 18.0	19.98	0.99	46	0.491	A	uncl	35.16	23.17
PDFJ011126.9-453416	0.102 ± 0.032	01 11 26.90	-45 34 16.4	18.69	0.99	35	5	51	6.14	0.190	A	sf	34.44	22.00
PDFJ011127.3-452106	0.164 ± 0.057	01 11 27.32	-45 21 06.1	19.39	0.99	30	14	0.375	B	sf	35.17	22.87
PDFJ011127.6-454946	0.163 ± 0.028	01 11 27.48	-45 49 45.8	18.53	1.00	11	2	0.343	A	sf	35.00	22.78
PDFJ011127.6-454815	0.416 ± 0.037	01 11 27.55	-45 48 15.1	18.62	1.00	8	1	0.279	A	uncl	34.71	22.99
PDFJ011128.5-455410	0.095 ± 0.030	01 11 28.48	-45 54 09.1	19.86	0.98	22	3	55	18.25	0.299	A	sf	34.42	22.41
PDFJ011129.6-455242	0.141 ± 0.030	01 11 29.54	-45 52 42.5	21.31	0.98	0.553	C	abs	...	23.20
PDFJ011131.5-450012	0.514 ± 0.167	01 11 31.34	-45 00 11.2	14.53	0.98	13	...	0.024	B	uncl	34.23	20.83
PDFJ011131.8-453813	0.090 ± 0.028	01 11 31.72	-45 38 14.1	20.41	0.99	56	46	0.538	B	sf	35.92	22.98
PDFJ011132.9-451756	0.173 ± 0.034	01 11 32.83	-45 17 57.1	17.76	1.00	2	1	27	11.86	0.126	A	sf	34.26	21.85
PDFJ011134.2-454609	0.086 ± 0.030	01 11 34.13	-45 46 09.4	19.46	1.00	28	2	0.420	A	Sey2	35.10	22.71
PDFJ011135.1-453245	0.229 ± 0.045	01 11 35.07	-45 32 44.8	16.07	1.00	8	...	0.089	A	sf	34.67	21.65
PDFJ011136.2-453424	0.257 ± 0.028	01 11 36.13	-45 34 24.4	19.05	0.99	19	2	0.376	A	Sey2	35.02	23.07
PDFJ011136.8-455806	0.111 ± 0.044	01 11 36.84	-45 58 05.2	17.76	0.99	...	5	39	15.31	0.090	A	sf	34.26	21.34
PDFJ011137.0-455254	0.094 ± 0.032	01 11 36.99	-45 52 52.4	18.34	0.94	...	3	37	14.37	0.188	A	sf	34.62	21.96
PDFJ011138.4-453357	0.114 ± 0.028	01 11 38.30	-45 33 57.3	20.77	0.99	84	50	0.670	A	Sey2	35.39	23.30
PDFJ011138.6-453856	0.184 ± 0.031	01 11 38.54	-45 38 55.0	19.56	0.99	12	5	46	18.26	0.370	A	sf	34.85	22.91
PDFJ011139.1-451618	0.309 ± 0.068	01 11 39.39	-45 16 17.2	18.90	0.26	0.377	A	abs	...	23.15
PDFJ011140.3-454713	0.528 ± 0.036	01 11 40.29	-45 47 13.4	19.43	0.97	2.239	B	Sey1	...	25.20
PDFJ011142.1-454659	0.099 ± 0.030	01 11 42.13	-45 47 00.2	18.88	1.00	37	18	82	6.34	0.301	A	sf	35.23	22.44
PDFJ011144.7-455210	0.404 ± 0.045	01 11 44.64	-45 52 11.7	18.52	0.99	52	2	0.298	A	Sey2	35.49	23.04
PDFJ011144.7-455649	0.078 ± 0.030	01 11 44.97	-45 56 51.2	21.16	0.65	44	0.612	C	uncl	35.11	23.04
PDFJ011146.3-454018	0.153 ± 0.035	01 11 46.31	-45 40 18.9	18.69	1.00	0.370	C	abs	...	22.83
PDFJ011147.6-451241	0.481 ± 0.055	01 11 47.58	-45 12 42.6	20.71	0.99	35	0.672	C	uncl	34.80	23.93
PDFJ011148.8-452438	0.097 ± 0.030	01 11 48.81	-45 24 38.4	21.48	0.99	26	0.649	C	uncl	34.73	23.20
PDFJ011149.5-455415	0.085 ± 0.032	01 11 49.44	-45 54 17.8	19.72	0.91	0.328	C	uncl	...	22.46
PDFJ011149.6-454207	0.155 ± 0.026	01 11 49.61	-45 42 07.2	20.92	1.00	0.743	C	uncl	...	23.54
PDFJ011150.2-453726	0.133 ± 0.028	01 11 50.21	-45 37 27.2	19.49	0.99	35	0.493	A	uncl	35.52	23.06
PDFJ011151.1-450218	3.216 ± 0.169	01 11 51.23	-45 02 14.8	18.12	0.11	0.272	A	abs	...	23.85
PDFJ011151.4-455644	0.320 ± 0.042	01 11 51.44	-45 56 44.5	18.43	0.99	40	3	29	11.22	0.090	A	sf	33.74	21.81
PDFJ011151.5-454446	0.079 ± 0.037	01 11 51.51	-45 44 44.5	21.26	0.82	...	9	0.496	A	sf	...	22.84
PDFJ011152.9-454023	0.143 ± 0.026	01 11 52.84	-45 40 24.4	19.15	0.99	31	1	16	9.63	0.228	A	sf	33.97	22.33
PDFJ011153.1-450430	0.305 ± 0.062	01 11 53.29	-45 04 31.2	17.54	0.95	0.000	-	star
PDFJ011153.5-455847	0.172 ± 0.049	01 11 53.45	-45 58 47.3	16.72	0.99	...	2	24	...	0.026	A	Sey2	33.99	20.41
PDFJ011154.2-453039	0.196 ± 0.030	01 11 54.19	-45 30 39.7	19.22	0.99	0.449	A	abs	...	23.13

Table 1—Continued

Radio source	S _{1.4 GHz} (mJy)	α (J2000)	δ (J2000)	R (mag)	\mathcal{R}	EW _{[OII]$\lambda 3727$} (Å)	EW _{Hβ} (Å)	EW _{Hα} (Å)	(H α /H β) _{obs}	z	Q	Class	log $L_{H\alpha}$ (W)	log $L_{1.4 \text{ GHz}}$ (W Hz $^{-1}$)
PDFJ011154.3-455409	0.156 ± 0.030	01 11 54.26	-45 54 09.2	18.30	0.99	9	3	51	19.20	0.136	A	sf	34.35	21.87
PDFJ011154.6-454639	0.104 ± 0.028	01 11 54.62	-45 46 39.5	20.18	1.00	0.342	A	abs	...	22.58
PDFJ011155.2-454212	0.242 ± 0.048	01 11 55.24	-45 42 13.9	18.10	0.99	11	2	50	8.25	0.229	A	sf	34.85	22.56
PDFJ011155.7-453443	0.102 ± 0.030	01 11 55.61	-45 34 42.9	17.73	0.99	...	4	39	7.39	0.126	A	sf	34.45	21.61
PDFJ011156.4-452915	0.143 ± 0.049	01 11 56.27	-45 29 16.2	17.69	0.98	16	...	0.111	B	uncl	34.01	21.65
PDFJ011156.4-455834	0.421 ± 0.047	01 11 56.38	-45 58 34.4	15.87	1.00	3	...	0.089	A	uncl	33.88	21.91
PDFJ011156.7-453345	0.150 ± 0.030	01 11 56.62	-45 33 45.3	19.79	0.99	35	0.540	C	uncl	34.98	23.20
PDFJ011156.7-445451	0.986 ± 0.142	01 11 56.69	-44 54 50.4	17.96	0.99	1.053	A	Sey1	...	24.70
PDFJ011156.7-454755	0.216 ± 0.041	01 11 56.71	-45 47 55.2	20.07	1.00	21	0.721	A	sf	35.58	23.66
PDFJ011158.7-455209	0.122 ± 0.030	01 11 58.71	-45 52 10.4	20.05	0.99	1.240	A	Sey1	...	23.97
PDFJ011202.3-460400	0.085 ± 0.032	01 12 02.39	-46 04 01.9	18.67	0.95	10	3	19	12.17	0.242	B	sf	34.70	22.16
PDFJ011203.0-454302	0.172 ± 0.056	01 12 02.78	-45 43 02.2	17.59	0.97	...	2	23	15.41	0.120	A	sf	34.28	21.80
PDFJ011204.0-455915	0.326 ± 0.039	01 12 03.98	-45 59 15.8	20.20	0.99	0.492	A	abs	...	23.44
PDFJ011204.7-454448	0.219 ± 0.026	01 12 04.62	-45 44 48.4	18.36	1.00	8	1	23	...	0.255	A	uncl	34.51	22.62
PDFJ011205.2-452133	0.104 ± 0.032	01 12 05.19	-45 21 33.8	19.18	0.99	...	16	110	8.50	0.256	A	uncl	34.98	22.30
PDFJ011206.4-444944	0.917 ± 0.317	01 12 06.34	-44 49 45.0	16.70	0.99	43	3	15	...	0.082	A	Sey2	33.96	22.18
PDFJ011206.7-451719	0.165 ± 0.036	01 12 06.65	-45 17 21.0	20.67	0.97	44	0.371	C	uncl	34.30	22.87
PDFJ011208.0-454838	0.431 ± 0.033	01 12 07.97	-45 48 38.8	21.99	0.99	38	0.857	C	uncl	33.61	24.13
PDFJ011208.2-451141	0.104 ± 0.040	01 12 08.17	-45 11 43.1	18.51	0.98	...	9	53	9.70	0.125	A	Sey2	34.35	21.62
PDFJ011210.3-455607	0.140 ± 0.058	01 12 10.37	-45 56 07.1	19.86	0.98	66	20	118	9.15	0.199	A	sf	34.59	22.19
PDFJ011210.6-463455	0.931 ± 0.118	01 12 10.69	-46 34 55.4	17.56	0.99	2	...	18	14.00	0.138	A	sf	34.32	22.66
PDFJ011211.5-462903	0.196 ± 0.068	01 12 11.54	-46 29 01.7	17.14	0.98	24	...	0.075	A	uncl	34.31	21.43
PDFJ011211.8-455818	0.161 ± 0.049	01 12 11.54	-45 58 18.3	20.78	0.56	23	0.552	C	uncl	34.80	23.25
PDFJ011212.1-454051	0.067 ± 0.026	01 12 12.09	-45 40 50.5	19.88	0.99	15	0.461	A	uncl	34.85	22.69
PDFJ011213.3-460322	0.119 ± 0.032	01 12 13.28	-46 03 21.2	19.33	0.99	31	15	0.364	A	sf	34.79	22.70
PDFJ011214.4-450843	0.113 ± 0.046	01 12 14.45	-45 08 43.6	21.39	0.99	9	0.328	B	abs	33.84	22.58
PDFJ011214.9-452706	0.129 ± 0.032	01 12 14.96	-45 27 06.8	20.38	0.99	0.546	B	Sey1	...	23.15
PDFJ011215.1-462339	0.325 ± 0.129	01 12 15.22	-46 23 40.4	17.93	0.99	4	1	13	...	0.255	A	sf	34.45	22.79
PDFJ011216.0-452550	0.193 ± 0.047	01 12 15.92	-45 25 50.2	17.05	1.00	8	...	0.089	B	uncl	33.88	21.57
PDFJ011216.5-454521	0.111 ± 0.028	01 12 16.45	-45 45 19.9	18.32	0.99	12	...	26	...	0.297	A	uncl	34.69	22.47
PDFJ011217.6-445836	1.487 ± 0.104	01 12 17.64	-44 58 36.9	20.72	0.99	0.703	B	abs	...	24.47
PDFJ011218.2-460715	0.290 ± 0.037	01 12 18.22	-46 07 15.2	18.96	0.99	21	4	0.407	B	sf	34.71	23.20
PDFJ011219.9-454926	0.104 ± 0.039	01 12 19.90	-45 49 26.9	19.67	0.99	65	22	104	8.70	0.241	A	sf	34.92	22.24
PDFJ011220.6-453949	0.079 ± 0.026	01 12 20.63	-45 39 48.6	19.85	0.83	29	6	0.465	B	sf	34.67	22.77
PDFJ011222.4-461738	0.315 ± 0.051	01 12 22.42	-46 17 38.8	21.75	0.99	30	0.856	C	uncl	35.33	24.00
PDFJ011224.9-455233	0.157 ± 0.028	01 12 24.79	-45 52 33.1	19.66	0.99	11	0.416	B	uncl	34.87	22.96
PDFJ011225.1-454700	0.150 ± 0.028	01 12 25.13	-45 47 00.2	18.54	0.99	42	15	150	4.90	0.236	A	sf	35.13	22.38
PDFJ011228.7-454959	0.196 ± 0.028	01 12 28.63	-45 50 00.1	20.34	0.99	12	0.298	A	uncl	34.26	22.72
PDFJ011229.8-445337	0.972 ± 0.136	01 12 29.81	-44 53 37.4	19.11	0.99	17	0.890	C	uncl	36.35	24.53
PDFJ011230.4-453417	0.168 ± 0.044	01 12 30.35	-45 34 18.6	18.68	0.99	11	...	33	...	0.292	A	uncl	34.80	22.64
PDFJ011231.3-454836	0.570 ± 0.127	01 12 31.63	-44 58 36.9	16.65	1.00	...	6	70	6.01	0.082	A	sf	34.68	21.97
PDFJ011232.0-460557	4.531 ± 0.061	01 12 32.04	-46 05 56.5	19.85	0.99	2.240	B	Sey1	...	26.14
PDFJ011232.2-450833	0.209 ± 0.058	01 12 32.12	-45 08 34.3	20.24	0.98	31	15	0.378	A	Sey2	34.77	22.99
PDFJ011235.8-445505	0.454 ± 0.191	01 12 35.67	-44 55 07.5	20.49	0.88	0.540	C	abs	...	23.68
PDFJ011235.8-460208	0.089 ± 0.033	01 12 35.83	-46 02 07.8	19.67	0.99	25	0.611	B	uncl	35.29	23.10
PDFJ011236.5-451842	2.351 ± 0.047	01 12 36.45	-45 18 42.1	17.70	1.00	0.235	A	abs	...	23.57
PDFJ011236.6-455618	0.111 ± 0.044	01 12 36.49	-45 56 20.4	19.87	0.95	50	14	0.374	A	sf	34.79	22.70
PDFJ011237.0-453853	0.074 ± 0.030	01 12 37.07	-45 38 53.2	19.09	0.99	0.138	C	abs	...	21.57
PDFJ011237.2-460041	0.147 ± 0.045	01 12 37.18	-46 00 40.8	19.11	0.99	...	12	66	7.41	0.241	B	sf	34.82	22.39
PDFJ011238.5-461851	0.214 ± 0.071	01 12 38.50	-46 18 53.9	18.63	0.92	23	5	52	15.79	0.185	A	sf	34.75	22.30

Table 1—Continued

Radio source	S _{1.4 GHz} (mJy)	α (J2000)	δ (J2000)	R (mag)	\mathcal{R}	EW _{[OIII]$\lambda 3727$} (Å)	EW _{Hβ} (Å)	EW _{Hα} (Å)	(H α /H β) _{obs}	z	Q	Class	log $L_{H\alpha}$ (W)	log $L_{1.4 \text{ GHz}}$ (W Hz $^{-1}$)
PDFJ011241.3-460323	0.214 ± 0.032	01 12 41.31	-46 03 23.3	19.36	0.99	49	12	15	5.77	0.313	A	uncl	34.97	22.81
PDFJ011241.5-460359	0.146 ± 0.051	01 12 41.43	-46 03 58.3	21.63	0.97	55	0.698	B	uncl	35.50	23.45
PDFJ011241.8-453706	0.545 ± 0.049	01 12 41.76	-45 37 06.5	17.70	0.99	0.234	A	abs	...	22.93
PDFJ011243.7-453744	0.317 ± 0.032	01 12 43.74	-45 37 43.6	18.59	0.99	0.235	A	abs	...	22.70
PDFJ011244.2-453315	0.332 ± 0.039	01 12 44.28	-45 33 15.0	21.26	0.99	5	0.539	B	abs	34.25	23.54
PDFJ011246.4-454049	0.106 ± 0.043	01 12 46.34	-45 40 47.6	19.63	0.98	40	6	0.374	B	sf	34.43	22.68
PDFJ011246.6-455852	0.134 ± 0.044	01 12 46.57	-45 58 52.6	19.26	0.99	57	8	0.360	A	sf	34.88	22.74
PDFJ011247.3-461323	0.442 ± 0.042	01 12 47.35	-46 13 22.9	20.92	0.99	28	0.816	B	Sey1	34.98	24.09
PDFJ011247.9-454450	0.847 ± 0.037	01 12 47.86	-45 44 50.1	18.30	0.99	82	2	15	...	0.239	A	uncl	34.36	23.14
PDFJ011250.9-461425	0.343 ± 0.070	01 12 51.10	-46 14 21.8	20.38	0.17	0.351	C	uncl	...	23.13
PDFJ011251.8-460034	0.378 ± 0.072	01 12 51.98	-46 00 35.9	17.53	0.97	48	5	28	14.18	0.132	A	sf	34.78	22.23
PDFJ011252.7-454345	1.558 ± 0.037	01 12 52.64	-45 43 44.9	15.43	0.99	0.076	A	abs	...	22.34
PDFJ011254.0-455210	0.086 ± 0.030	01 12 53.86	-45 52 09.0	21.21	0.91	111	0.613	B	uncl	35.40	23.09
PDFJ011255.4-455907	0.268 ± 0.032	01 12 55.58	-45 59 06.1	19.47	0.96	37	8	0.445	A	sf	35.36	23.26
PDFJ011257.4-451747	0.141 ± 0.045	01 12 57.42	-45 17 46.0	16.62	0.98	0.144	B	uncl	...	21.89
PDFJ011259.8-452419	0.091 ± 0.034	01 12 59.84	-45 24 18.3	20.02	0.99	83	9	0.369	A	sf	34.71	22.60
PDFJ011300.0-454119	0.143 ± 0.042	01 13 00.02	-45 41 20.7	17.22	0.98	0.096	B	abs	...	21.51
PDFJ011303.9-453008	0.382 ± 0.044	01 13 03.88	-45 30 08.8	16.42	0.99	...	2	26	10.01	0.086	A	sf	34.37	21.84
PDFJ011306.0-462603	0.631 ± 0.089	01 13 06.00	-46 26 03.4	17.18	0.99	...	12	102	...	0.066	A	sf	34.42	21.82
PDFJ011307.7-460532	0.100 ± 0.038	01 13 07.75	-46 05 31.8	18.96	0.99	10	-2	0.368	B	abs	34.15	22.64
PDFJ011308.2-455749	0.284 ± 0.042	01 13 08.21	-45 57 49.5	19.59	0.99	24	1	0.447	A	Sey2	35.04	23.29
PDFJ011310.8-461015	0.188 ± 0.056	01 13 10.60	-46 10 14.8	19.71	0.97	25	0.272	C	uncl	33.80	22.61
PDFJ011311.0-450145	0.539 ± 0.135	01 13 10.97	-45 01 45.5	16.37	0.99	...	4	63	7.27	0.082	A	Sey2	34.75	21.94
PDFJ011313.7-460156	0.405 ± 0.034	01 13 13.76	-46 01 56.6	15.95	0.99	0.134	A	abs	...	22.27
PDFJ011314.7-453701	0.274 ± 0.038	01 13 14.69	-45 37 01.0	18.98	0.99	0.368	A	abs	...	23.08
PDFJ011314.8-454050	1.027 ± 0.045	01 13 14.70	-45 40 51.1	21.78	0.99	49	0.985	C	uncl	35.65	24.65
PDFJ011315.2-454523	0.109 ± 0.030	01 13 15.27	-45 45 23.7	21.06	0.99	28	0.368	C	uncl	34.50	22.68
PDFJ011315.8-445919	0.326 ± 0.104	01 13 15.70	-44 59 19.0	17.34	0.99	16	1	52	14.19	0.235	A	Sey2	35.10	22.71
PDFJ011318.6-454716	0.147 ± 0.048	01 13 18.47	-45 47 14.6	19.17	0.92	18	3	0.332	A	sf	34.30	22.70
PDFJ011318.5-453359	0.259 ± 0.041	01 13 18.45	-45 34 00.5	17.81	0.99	...	4	30	12.49	0.230	A	sf	35.00	22.59
PDFJ011320.6-455524	0.260 ± 0.030	01 13 20.61	-45 55 24.3	19.70	0.99	42	0.419	A	uncl	34.74	23.18
PDFJ011321.1-461241	0.347 ± 0.053	01 13 21.20	-46 12 41.5	21.42	0.99	35	0.818	A	uncl	35.36	23.99
PDFJ011321.2-454446	0.141 ± 0.044	01 13 21.20	-45 44 45.3	20.92	0.99	0.229	C	uncl	...	22.32
PDFJ011321.7-464011	0.479 ± 0.188	01 13 21.64	-46 40 07.8	19.97	0.03	21	0.425	C	uncl	34.86	23.46
PDFJ011323.2-461130	0.135 ± 0.044	01 13 23.32	-46 11 31.9	18.53	0.98	5	...	18	...	0.158	A	Sey2	33.85	21.95
PDFJ011324.6-452251	0.281 ± 0.107	01 13 24.92	-45 22 52.6	16.23	<0.01	...	3	26	8.15	0.030	A	sf	-0.03	20.76
PDFJ011325.2-461533	0.875 ± 0.062	01 13 25.18	-46 15 32.5	18.14	0.99	4	...	0.254	B	abs	...	23.22
PDFJ011325.4-454216	0.082 ± 0.030	01 13 25.45	-45 42 17.1	18.81	0.99	19	4	35	9.39	0.121	A	sf	33.93	21.48
PDFJ011325.9-454909	0.241 ± 0.047	01 13 25.89	-45 49 10.1	17.73	0.99	19	6	46	7.37	0.253	A	uncl	35.20	22.65
PDFJ011326.9-453119	0.143 ± 0.043	01 13 26.83	-45 31 20.3	18.85	0.99	18	6	0.372	C	sf	34.69	22.80
PDFJ011326.9-462423	0.781 ± 0.076	01 13 26.99	-46 24 22.4	18.05	0.99	6	0.254	A	abs	34.80	23.17
PDFJ011329.5-453719	0.345 ± 0.046	01 13 29.54	-45 37 18.4	20.90	0.99	0.693	A	abs	...	23.82
PDFJ011330.2-460956	0.223 ± 0.063	01 13 30.30	-46 09 54.9	17.56	0.94	25	6	13	8.20	0.186	A	sf	34.84	22.32
PDFJ011330.9-452121	0.784 ± 0.046	01 13 30.92	-45 21 21.4	18.25	0.99	0.327	A	abs	...	23.42
PDFJ011331.8-460205	0.626 ± 0.083	01 13 31.75	-46 02 06.0	15.93	0.99	...	1	18	13.32	0.090	A	sf	34.52	22.09
PDFJ011333.4-453841	0.472 ± 0.038	01 13 33.36	-45 38 40.8	18.47	0.99	116	43	155	6.03	0.276	A	sf	35.45	23.03
PDFJ011335.3-460047	0.413 ± 0.116	01 13 35.48	-46 00 47.9	19.50	0.96	...	8	51	13.23	0.234	A	sf	34.76	22.81
PDFJ011335.6-460955	0.646 ± 0.080	01 13 35.52	-46 09 54.5	16.16	0.99	...	1	18	33.42	0.085	A	sf	34.48	22.06
PDFJ011338.9-460635	0.211 ± 0.089	01 13 38.81	-46 06 33.5	19.24	0.97	24	6	0.448	A	sf	34.88	23.16
PDFJ011341.4-460113	0.140 ± 0.040	01 13 41.41	-46 01 13.5	16.80	0.99	0.132	B	abs	...	21.80

23

Table 1—Continued

Radio source	$S_{1.4 \text{ GHz}}$ (mJy)	α (J2000)	δ (J2000)	R (mag)	\mathcal{R}	$\text{EW}_{[\text{OII}]\lambda 3727}$ (Å)	$\text{EW}_{\text{H}\beta}$ (Å)	$\text{EW}_{\text{H}\alpha}$ (Å)	$(\text{H}\alpha/\text{H}\beta)_{\text{obs}}$	z	Q	Class	$\log L_{\text{H}\alpha}$ (W)	$\log L_{1.4 \text{ GHz}}$ (W Hz $^{-1}$)
PDFJ011343.9-455616	1.164 ± 0.046	01 13 43.64	-45 56 17.5	20.24	0.42	29	...	30	...	0.300	B	uncl	34.11	23.50
PDFJ011345.5-452612	0.131 ± 0.042	01 13 45.47	-45 26 08.9	16.80	0.24	0.089	B	uncl	...	21.40
PDFJ011348.6-455019	0.898 ± 0.047	01 13 48.65	-45 50 19.0	16.23	0.99	...	2	6	10.43	0.057	A	sf	33.60	21.84
PDFJ011349.1-454050	0.297 ± 0.043	01 13 49.22	-45 40 50.6	19.96	0.99	1.837	B	Sey1	...	24.75
PDFJ011353.3-445335	1.191 ± 0.201	01 13 53.28	-44 53 34.9	16.52	0.99	0.147	A	abs	...	22.83
PDFJ011355.1-452716	2.513 ± 0.070	01 13 55.06	-45 27 15.8	15.51	0.99	...	-4	0.090	A	abs	...	22.70
PDFJ011356.7-453829	0.129 ± 0.057	01 13 56.77	-45 38 28.2	16.75	0.98	...	1	12	18.58	0.094	A	uncl	34.13	21.45
PDFJ011358.5-450353	1.611 ± 0.134	01 13 58.36	-45 03 56.9	19.54	<0.01	0.309	C	uncl	...	23.67
PDFJ011400.3-454752	0.282 ± 0.059	01 14 00.51	-45 47 52.0	18.63	0.90	45	20	70	4.44	0.071	A	sf	34.28	21.53
PDFJ011403.7-455912	0.107 ± 0.036	01 14 03.76	-45 59 11.3	19.42	0.99	13	8	0.339	A	sf	34.19	22.59
PDFJ011403.8-451837	0.272 ± 0.066	01 14 03.77	-45 18 37.1	20.77	0.99	39	0.278	B	uncl	34.19	22.80
PDFJ011404.6-455700	0.650 ± 0.044	01 14 04.66	-45 57 00.5	19.50	0.99	0.374	A	abs	...	23.47
PDFJ011405.3-461512	1.257 ± 0.069	01 14 05.30	-46 15 11.9	15.53	0.99	...	5	51	15.78	0.031	A	sf	34.26	21.44
PDFJ011405.7-450652	0.229 ± 0.088	01 14 05.86	-45 06 50.9	17.67	0.98	...	14	109	3.75	0.076	A	sf	34.43	21.51
PDFJ011406.1-454156	0.102 ± 0.034	01 14 06.05	-45 41 56.4	20.67	0.99	...	21	190	3.36	0.200	B	sf	34.01	22.05
PDFJ011407.4-460527	0.152 ± 0.044	01 14 07.39	-46 05 27.2	20.14	0.99	63	...	0.249	B	uncl	34.50	22.44
PDFJ011407.5-4541450	21.824 ± 0.292	01 14 07.60	-45 14 47.9	15.51	0.89	...	-3	0.089	A	abs	...	23.63
PDFJ011407.6-451448	26.996 ± 0.351	01 14 07.60	-45 14 47.9	15.51	0.95	...	-3	0.089	A	abs	...	23.72
PDFJ011408.2-460943	0.157 ± 0.044	01 14 08.21	-46 09 44.7	18.84	0.99	23	...	26	...	0.234	A	uncl	34.74	22.39
PDFJ011408.4-445648	0.585 ± 0.126	01 14 08.36	-44 56 47.9	17.11	0.98	0.253	A	abs	...	23.04
PDFJ011408.8-444849	1.266 ± 0.203	01 14 08.84	-44 48 50.0	16.42	0.99	0.147	A	abs	...	22.86
PDFJ011409.5-453246	0.364 ± 0.056	01 14 09.48	-45 32 44.6	19.96	0.98	15	0.596	A	uncl	35.29	23.69
PDFJ011411.2-452044	0.564 ± 0.131	01 14 11.07	-45 20 44.6	15.63	0.98	...	5	20	6.92	0.030	A	sf	33.78	21.06
PDFJ011411.5-461733	0.745 ± 0.117	01 14 11.73	-46 17 33.4	15.65	0.95	...	5	30	9.74	0.030	A	sf	33.89	21.19
PDFJ011411.6-460420	0.207 ± 0.069	01 14 11.88	-46 04 19.4	20.31	0.37	13	0.412	C	uncl	33.70	23.07
PDFJ011413.9-455459	0.091 ± 0.038	01 14 13.90	-45 55 00.7	19.36	0.99	16	3	15	11.91	0.247	B	uncl	34.05	22.21
PDFJ011414.1-454700	0.130 ± 0.049	01 14 14.26	-45 47 03.0	19.21	0.73	13	0.342	B	uncl	34.36	22.68
PDFJ011414.5-464243	7.697 ± 0.231	01 14 14.47	-46 42 44.2	15.95	0.99	...	-4	0.117	A	abs	...	23.43
PDFJ011414.6-451952	1.821 ± 0.060	01 14 14.65	-45 19 51.7	16.31	0.99	8	1	16	8.58	0.123	A	Sey2	34.48	22.85
PDFJ011414.7-452553	0.309 ± 0.115	01 14 14.72	-45 25 53.6	19.64	0.99	19	...	0.235	B	uncl	34.10	22.69
PDFJ011415.0-454824	1.422 ± 0.057	01 14 15.05	-45 48 25.1	15.49	0.99	...	9	55	7.22	0.025	A	sf	34.07	21.30
PDFJ011415.8-453147	0.316 ± 0.040	01 14 15.66	-45 31 47.7	16.88	0.99	18	8	79	4.35	0.077	A	sf	34.59	21.66
PDFJ011416.5-452713	0.222 ± 0.042	01 14 16.48	-45 27 13.0	18.81	0.99	...	6	69	9.57	0.189	A	Sey2	34.56	22.34
PDFJ011417.3-451436	0.548 ± 0.165	01 14 17.26	-45 14 34.4	21.12	0.83	50	42	0.283	B	sf	34.15	23.12
PDFJ011419.5-453154	0.336 ± 0.044	01 14 19.43	-45 31 54.0	20.01	0.99	22	0.827	A	Sey1	35.26	23.99
PDFJ011423.0-453430	1.636 ± 0.050	01 14 23.00	-45 34 29.9	21.37	0.99	162	0.656	A	uncl	35.80	24.44
PDFJ011425.1-450448	0.687 ± 0.126	01 14 25.19	-45 04 48.1	15.60	0.99	...	-4	6	...	0.122	A	sf	35.08	22.42
PDFJ011426.4-455224	0.394 ± 0.054	01 14 26.52	-45 52 22.9	18.89	0.97	30	0.459	A	uncl	35.69	23.46
PDFJ011428.4-453637	0.633 ± 0.049	01 14 28.44	-45 36 37.0	19.47	0.99	21	0.406	A	sf	35.17	23.54
PDFJ011428.8-452821	1.819 ± 0.067	01 14 28.84	-45 28 21.4	21.16	0.99	0.693	C	abs	...	24.54
PDFJ011432.9-452400	0.217 ± 0.058	01 14 32.93	-45 24 01.2	18.76	0.99	53	14	0.333	A	sf	35.67	22.88
PDFJ011434.0-452601	0.145 ± 0.048	01 14 33.93	-45 26 01.1	21.05	0.99	0.336	B	uncl	...	22.71
PDFJ011434.7-453807	0.110 ± 0.042	01 14 34.80	-45 38 06.6	20.22	0.99	17	...	32	...	0.238	B	uncl	34.25	22.25
PDFJ011435.8-452951	0.243 ± 0.081	01 14 36.02	-45 29 51.9	19.55	0.96	13	4	0.273	B	sf	34.21	22.73
PDFJ011436.8-445126	1.709 ± 0.173	01 14 36.76	-44 51 26.4	19.73	0.99	54	10	0.380	A	Sey2	35.22	23.90
PDFJ011437.2-461751	0.275 ± 0.080	01 14 37.25	-46 17 52.1	19.66	0.29	0.355	C	uncl	34.86	23.04
PDFJ011438.9-454027	1.098 ± 0.072	01 14 38.88	-45 40 27.2	21.18	0.99	0.662	C	abs	...	24.27
PDFJ011440.7-461029	0.184 ± 0.068	01 14 40.67	-46 10 27.4	17.63	0.91	2	1.165	C	Sey1	35.69	24.08
PDFJ011440.7-451205	0.438 ± 0.100	01 14 40.69	-45 12 04.2	20.60	0.99	0.898	C	Sey1	...	24.19
PDFJ011442.3-452148	0.384 ± 0.084	01 14 42.34	-45 21 49.5	17.57	0.99	...	6	50	9.46	0.121	A	sf	34.60	22.15

Table 1—Continued

Radio source	$S_{1.4 \text{ GHz}}$ (mJy)	α (J2000)	δ (J2000)	R (mag)	\mathcal{R}	$\text{EW}_{[\text{OII}]\lambda 3727}$ (Å)	$\text{EW}_{\text{H}\beta}$ (Å)	$\text{EW}_{\text{H}\alpha}$ (Å)	$(\text{H}\alpha/\text{H}\beta)_{\text{obs}}$	z	Q	Class	$\log L_{\text{H}\alpha}$ (W)	$\log L_{1.4 \text{ GHz}}$ (W Hz $^{-1}$)
PDFJ011442.3-452918	0.304 ± 0.048	01 14 42.50	-45 29 17.1	18.30	0.94	13	3	42	19.45	0.187	A	sf	34.70	22.46
PDFJ011442.7-452421	1.099 ± 0.087	01 14 42.71	-45 24 21.4	15.49	0.99	...	-3	0.093	A	abs	...	22.37
PDFJ011443.1-455416	0.780 ± 0.053	01 14 43.08	-45 54 16.2	20.75	0.99	84	0.526	B	uncl	35.55	23.89
PDFJ011444.0-453611	0.184 ± 0.046	01 14 44.07	-45 36 11.4	22.20	0.99	79	1.163	C	uncl	35.86	24.08
PDFJ011450.9-454456	0.125 ± 0.044	01 14 50.83	-45 44 55.3	21.32	0.99	19	0.463	C	uncl	34.19	22.97
PDFJ011453.7-455821	0.584 ± 0.079	01 14 53.79	-45 58 21.3	17.53	0.99	13	3	41	6.99	0.236	A	sf	35.05	22.97
PDFJ011454.1-454707	0.353 ± 0.069	01 14 54.05	-45 47 05.5	19.21	0.96	9	4	28	7.73	0.216	A	sf	34.12	22.67
PDFJ011457.9-450616	0.640 ± 0.134	01 14 57.84	-45 06 15.4	19.18	0.99	12	...	94	...	0.334	A	sf	35.06	23.35
PDFJ011459.9-445756	1.181 ± 0.241	01 14 59.90	-44 57 57.7	18.05	0.99	9	1	34	13.49	0.224	A	Sey2	34.59	23.23
PDFJ011503.5-454239	0.135 ± 0.056	01 15 03.44	-45 42 36.3	19.42	0.71	38	...	0.133	B	uncl	33.89	21.79
PDFJ011504.9-454943	0.478 ± 0.075	01 15 04.93	-45 49 44.5	20.88	0.98	0.000	-	star
PDFJ011508.3-455410	0.249 ± 0.081	01 15 08.37	-45 54 12.3	18.68	0.98	8	4	24	15.38	0.235	B	sf	34.51	22.60
PDFJ011508.4-453425	0.325 ± 0.056	01 15 08.56	-45 34 25.6	19.51	0.98	...	1	0.189	B	uncl	...	22.50
PDFJ011510.7-462305	1.597 ± 0.134	01 15 10.74	-46 23 06.5	20.34	0.56	14	0.633	C	uncl	34.74	24.39
PDFJ011513.2-461527	0.369 ± 0.126	01 15 13.28	-46 15 27.4	16.98	0.99	...	-2	7	...	0.170	A	sf	34.21	22.46
PDFJ011518.8-445510	5.462 ± 0.293	01 15 18.82	-44 55 10.3	14.22	0.99	...	8	69	5.02	0.031	A	sf	34.85	22.09
PDFJ011521.9-455216	1.153 ± 0.085	01 15 21.89	-45 52 15.3	18.89	0.99	0.373	A	abs	...	23.71
PDFJ011522.1-455611	0.200 ± 0.072	01 15 22.09	-45 56 11.3	19.54	0.99	0.959	B	Sey1	...	23.92
PDFJ011525.8-450250	0.807 ± 0.193	01 15 25.87	-45 02 47.0	19.12	0.21	0.316	A	abs	...	23.40
PDFJ011527.2-455523	0.981 ± 0.122	01 15 27.07	-45 55 23.9	20.04	0.98	23	0.527	B	uncl	35.27	23.99
PDFJ011527.1-453101	1.005 ± 0.094	01 15 27.21	-45 31 01.4	18.83	0.57	0.000	-	star
PDFJ011534.2-454433	0.210 ± 0.082	01 15 34.18	-45 44 31.6	18.61	0.93	...	13	30	2.90	0.162	B	sf	34.26	22.17
PDFJ011538.1-450023	1.525 ± 0.264	01 15 37.86	-45 00 21.8	17.15	0.32	0.000	-	star
PDFJ011539.6-455344	2.162 ± 0.142	01 15 39.59	-45 53 44.4	22.18	0.99	1.352	C	Sey1	...	25.30
PDFJ011544.8-455550	39.817 ± 0.422	01 15 44.83	-45 55 49.6	16.00	0.99	6	...	0.104	A	sf	34.83	24.03
PDFJ011545.4-454936	0.255 ± 0.098	01 15 45.41	-45 49 36.6	19.03	0.99	3	0.373	A	abs	34.42	23.06
PDFJ011548.2-460948	9.191 ± 0.173	01 15 48.16	-46 09 48.5	20.75	0.99	1.345	B	Sey1	...	25.93
PDFJ011548.5-453049	0.428 ± 0.098	01 15 48.56	-45 30 49.2	20.47	0.99	1.151	B	Sey1	...	24.43
PDFJ011549.8-451311	1.835 ± 0.186	01 15 49.77	-45 13 10.4	17.99	0.99	0.324	A	abs	...	23.78
PDFJ011551.8-455423	1.164 ± 0.152	01 15 51.95	-45 54 22.4	20.20	0.97	5	0.460	A	abs	34.39	23.93
PDFJ011600.2-452914	0.261 ± 0.112	01 16 00.20	-45 29 13.3	17.59	0.98	...	9	78	5.50	0.089	A	sf	34.42	21.71
PDFJ011604.1-455017	0.453 ± 0.148	01 16 04.12	-45 50 16.5	17.94	0.99	0.371	A	abs	...	23.30
PDFJ011610.9-455822	0.920 ± 0.276	01 16 10.67	-45 58 22.4	14.22	0.93	...	-4	5	...	0.025	A	sf	33.51	21.13
PDFJ011612.4-454849	0.250 ± 0.098	01 16 12.49	-45 48 47.6	19.22	0.97	0.460	C	abs	...	23.26
PDFJ011614.4-451204	4.247 ± 0.259	01 16 14.43	-45 12 04.5	18.30	0.99	0.324	A	abs	...	24.14
PDFJ011617.1-460302	0.885 ± 0.129	01 16 17.09	-46 03 01.9	16.80	0.99	28	2	67	18.43	0.201	A	Sey2	35.30	23.00
PDFJ011625.9-451502	1.071 ± 0.176	01 16 25.93	-45 15 01.5	19.82	0.99	51	0.419	B	sf	35.46	23.80
PDFJ011633.8-461402	0.358 ± 0.106	01 16 33.84	-46 14 04.6	16.03	0.96	...	1	26	16.70	0.029	A	sf	33.65	20.82
PDFJ011634.7-461744	0.737 ± 0.112	01 16 34.75	-46 17 43.9	15.94	0.99	...	5	81	...	0.106	A	sf	35.26	22.32
PDFJ011635.9-461643	0.400 ± 0.110	01 16 35.95	-46 16 42.4	19.16	0.99	0.535	A	abs	...	23.62
PDFJ011652.1-455611	0.368 ± 0.130	01 16 52.11	-45 56 11.8	17.87	0.99	11	4	73	10.03	0.203	A	sf	35.02	22.62
PDFJ011654.8-445836	1.353 ± 0.268	01 16 54.74	-44 58 36.4	19.68	0.99	162	3	0.370	A	uncl	35.88	23.78
PDFJ011655.5-455409	0.406 ± 0.134	01 16 55.53	-45 54 05.8	18.03	0.41	16	...	35	...	0.119	A	uncl	34.16	22.16
PDFJ011700.8-455810	0.909 ± 0.128	01 17 00.78	-45 58 10.2	20.82	0.99	0.806	C	Sey1	...	24.39
PDFJ011703.3-462431	1.859 ± 0.279	01 17 03.20	-46 24 32.5	14.90	0.96	12	...	0.030	B	uncl	33.83	21.59
PDFJ011708.6-462715	0.832 ± 0.275	01 17 08.57	-46 27 12.2	15.55	0.60	10	...	0.051	B	uncl	33.98	21.71
PDFJ011711.6-455747	1.914 ± 0.129	01 17 11.59	-45 57 46.6	20.76	0.99	160	13	0.270	B	uncl	34.39	23.61
PDFJ011719.4-455959	0.573 ± 0.130	01 17 19.44	-45 59 59.1	18.34	0.99	...	5	81	8.24	0.254	A	Sey2	34.95	23.03
PDFJ011720.7-445924	15.102 ± 0.621	01 17 20.91	-44 59 24.0	21.09	0.96	29	0.792	A	uncl	35.57	25.60
PDFJ011722.3-454649	0.694 ± 0.130	01 17 22.18	-45 46 49.2	17.67	0.99	0.232	C	uncl	...	23.03

Table 1—Continued

Radio source	$S_{1.4 \text{ GHz}}$ (mJy)	α (J2000)	δ (J2000)	R (mag)	\mathcal{R}	$\text{EW}_{[\text{OII}]\lambda 3727}$ (Å)	$\text{EW}_{\text{H}\beta}$ (Å)	$\text{EW}_{\text{H}\alpha}$ (Å)	$(\text{H}\alpha/\text{H}\beta)_{\text{obs}}$	z	Q	Class	$\log L_{\text{H}\alpha}$ (W)	$\log L_{1.4 \text{ GHz}}$ (W Hz $^{-1}$)
PDFJ011722.6-455021	0.378 ± 0.132	01 17 22.60	-45 50 22.6	16.38	0.99	0.125	A	abs	...	22.18
PDFJ011725.3-460548	0.987 ± 0.199	01 17 25.39	-46 05 47.7	16.80	0.98	...	3	72	7.39	0.090	A	sf	34.72	22.29
PDFJ011730.5-460639	0.865 ± 0.114	01 17 30.57	-46 06 40.0	19.82	0.99	9	0.527	A	sf	34.95	23.94
PDFJ011731.2-453818	0.442 ± 0.148	01 17 31.19	-45 38 20.0	20.49	0.99	0.536	A	abs	...	23.66
PDFJ011732.9-461126	0.398 ± 0.122	01 17 32.90	-46 11 25.8	17.58	0.99	0.236	A	abs	...	22.80
PDFJ011741.7-461104	0.424 ± 0.122	01 17 41.68	-46 11 03.3	16.55	0.99	...	1	46	...	0.104	A	uncl	34.75	22.06
PDFJ011800.9-453832	2.890 ± 0.167	01 18 01.02	-45 38 29.1	17.06	0.35	0.000	-	star
PDFJ011804.6-455808	1.055 ± 0.146	01 18 04.65	-45 58 07.0	20.77	0.99	7	0.803	A	uncl	35.10	24.46
PDFJ011806.8-451901	0.717 ± 0.204	01 18 06.83	-45 19 01.6	18.43	0.99	0.301	A	abs	...	23.30
PDFJ011807.7-454538	0.683 ± 0.156	01 18 07.82	-45 45 37.6	18.98	0.99	11	0.370	B	uncl	34.26	23.48
PDFJ011812.1-454524	0.608 ± 0.190	01 18 12.11	-45 45 24.4	18.97	0.99	37	13	0.370	A	sf	35.53	23.43
PDFJ011820.7-453939	21.980 ± 0.297	01 18 20.76	-45 39 38.9	15.94	0.99	0.132	A	abs	...	23.99
PDFJ011831.2-453504	5.817 ± 0.216	01 18 31.25	-45 35 04.1	18.68	0.99	30	...	45	...	0.334	B	uncl	34.74	24.31
PDFJ011856.2-454250	2.589 ± 0.182	01 18 56.32	-45 42 48.9	19.79	0.95	15	0.435	C	uncl	34.28	24.22
PDFJ011901.0-460314	1.196 ± 0.202	01 19 00.79	-46 03 13.3	20.14	0.96	0.338	B	abs	...	23.63
PDFJ011906.8-453004	0.753 ± 0.254	01 19 06.76	-45 30 03.2	20.57	0.98	0.560	A	uncl	...	23.94
PDFJ011909.9-453015	0.628 ± 0.254	01 19 09.83	-45 30 15.6	16.21	0.99	31	...	0.146	A	uncl	35.59	22.54
PDFJ011919.8-454628	1.024 ± 0.196	01 19 19.89	-45 46 29.2	19.73	0.99	7	0.376	A	uncl	34.52	23.67
PDFJ011925.8-454339	1.511 ± 0.217	01 19 25.84	-45 43 38.9	16.50	0.99	0.148	A	abs	...	22.94
PDFJ011932.4-454935	3.803 ± 0.396	01 19 32.42	-45 49 33.5	17.31	0.98	...	-5	0.236	B	abs	...	23.78
PDFJ010951.2-455624	0.690 ± 0.029	01 09 50.89	-45 56 27.1	18.86	0.05	0.255	B	abs	...	23.12

Table 2. Galaxy populations at faint 1.4 GHz flux levels

Galaxy type	$S_{1.4\text{ GHz}} \geq 1.0$ (mJy)	$0.2 \leq S_{1.4\text{ GHz}} < 1.0$ (mJy)	$S_{1.4\text{ GHz}} < 0.2$ (mJy)
star-forming	11%	37%	36%
absorption	47%	20%	12%
Seyfert	14%	14%	7%
unclassified	28%	29%	45%

Table 3. Radio (1.4 GHz) Luminosity Function for star-forming galaxies

$\log L_{\text{1.4 GHz}}$ (W Hz $^{-1}$)	$\Phi^{z=0-0.2}(L_{\text{1.4 GHz}})$ (Mpc $^{-3}$ dex $^{-1}$)	$\Phi^{z=0.2-0.5}(L_{\text{1.4 GHz}})$ (Mpc $^{-3}$ dex $^{-1}$)
20.6	$(2.0 \pm 1.4) \times 10^{-2}$...
21.0	$(8.4 \pm 4.6) \times 10^{-3}$...
21.4	$(4.0 \pm 1.7) \times 10^{-3}$...
21.8	$(2.2 \pm 0.7) \times 10^{-3}$...
22.2	$(6.8 \pm 2.4) \times 10^{-4}$...
22.6	$(2.4 \pm 1.1) \times 10^{-4}$...
22.7	...	$(3.5 \pm 1.3) \times 10^{-4}$
23.1	...	$(1.2 \pm 0.6) \times 10^{-4}$
23.5	...	$(1.3 \pm 0.7) \times 10^{-5}$

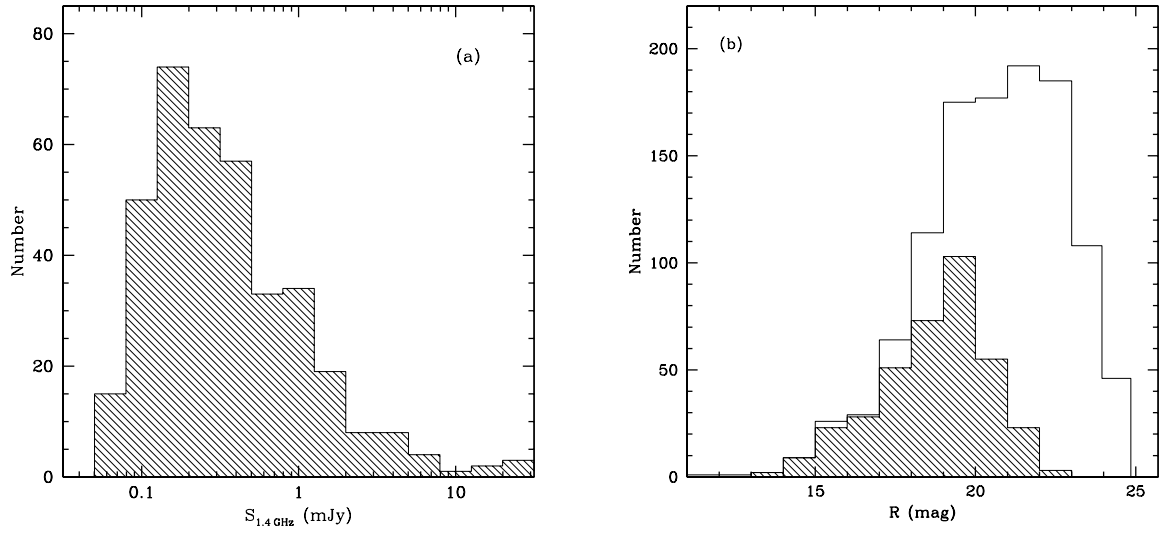


Fig. 1.— Radio (1.4 GHz) flux density distribution (a) and R -band distribution (b) for the 371 optical counterparts of faint radio sources with a spectroscopic redshift determination. The open histogram in (b) represents the R -band magnitude distribution for the full sample of optical identifications of the Phoenix Deep Survey.

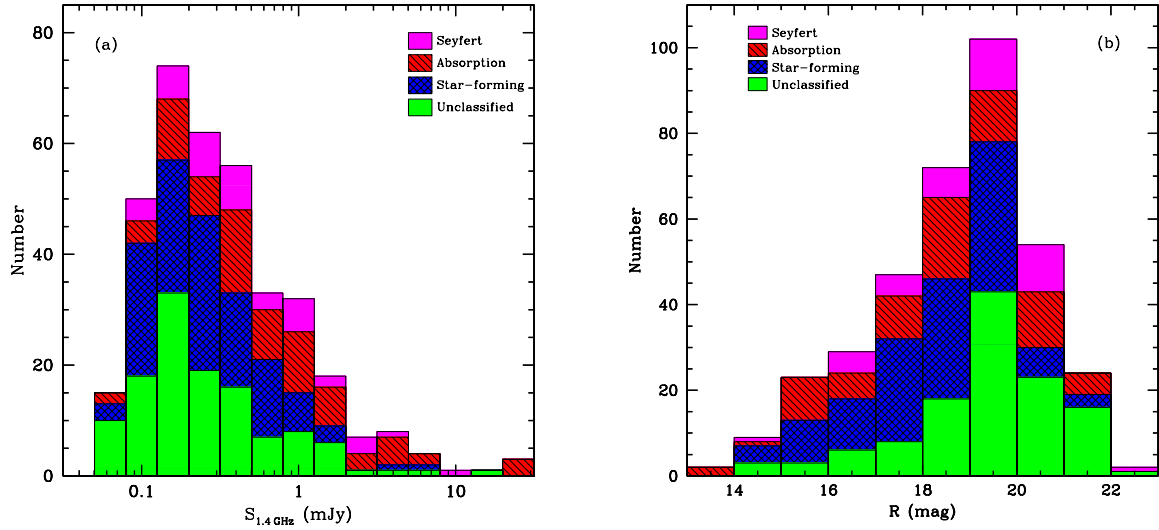


Fig. 2.— Radio (1.4 GHz) flux density distribution (a) and R -band distribution (b) for the extragalactic sources in the present survey according to spectral type.

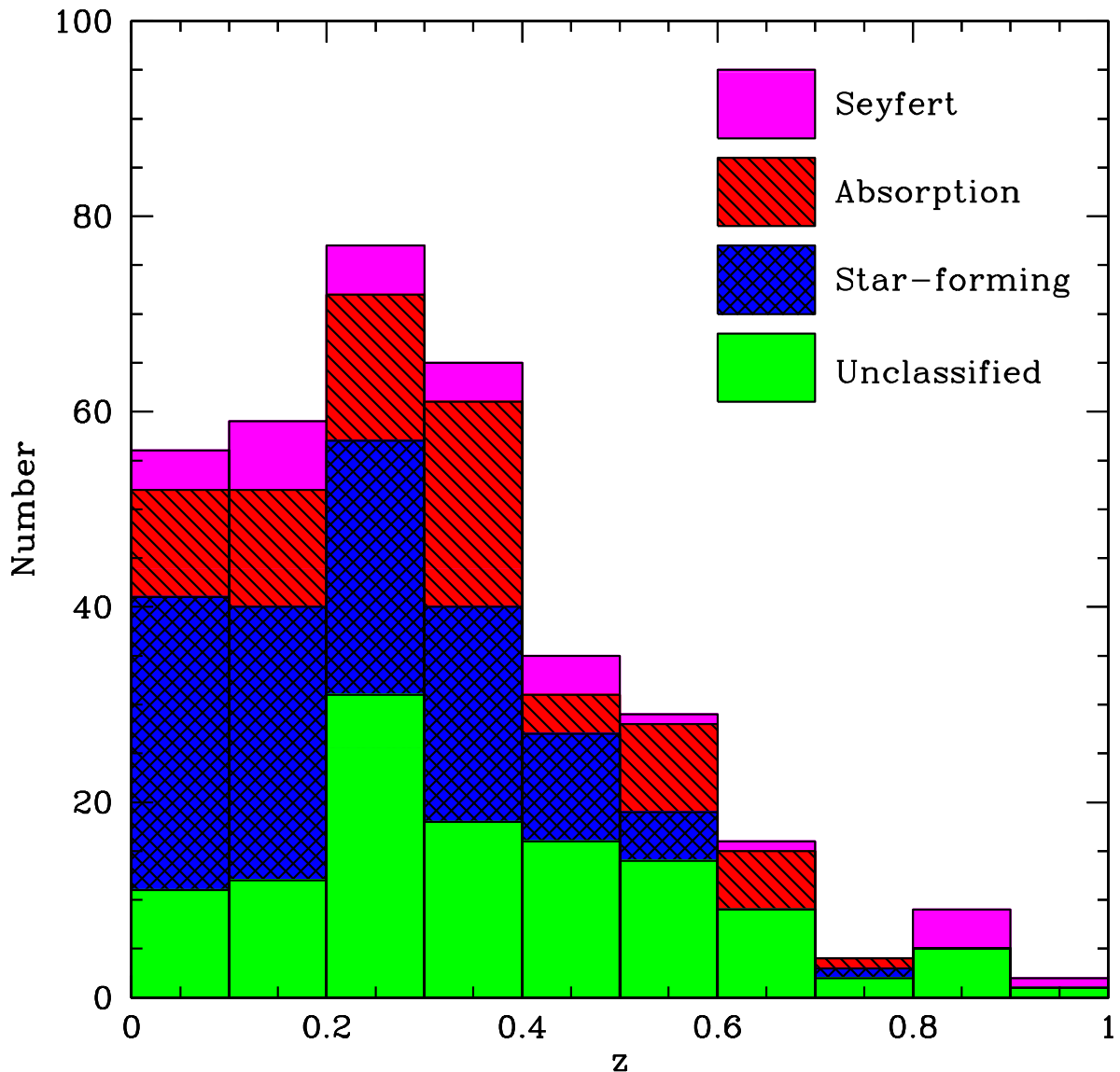


Fig. 3.— Redshift distribution for the faint radio galaxies in the sample according to spectral type. Eleven Seyfert 1 and one unclassified galaxy with $1.0 < z < 3.1$ are not shown in this Figure.

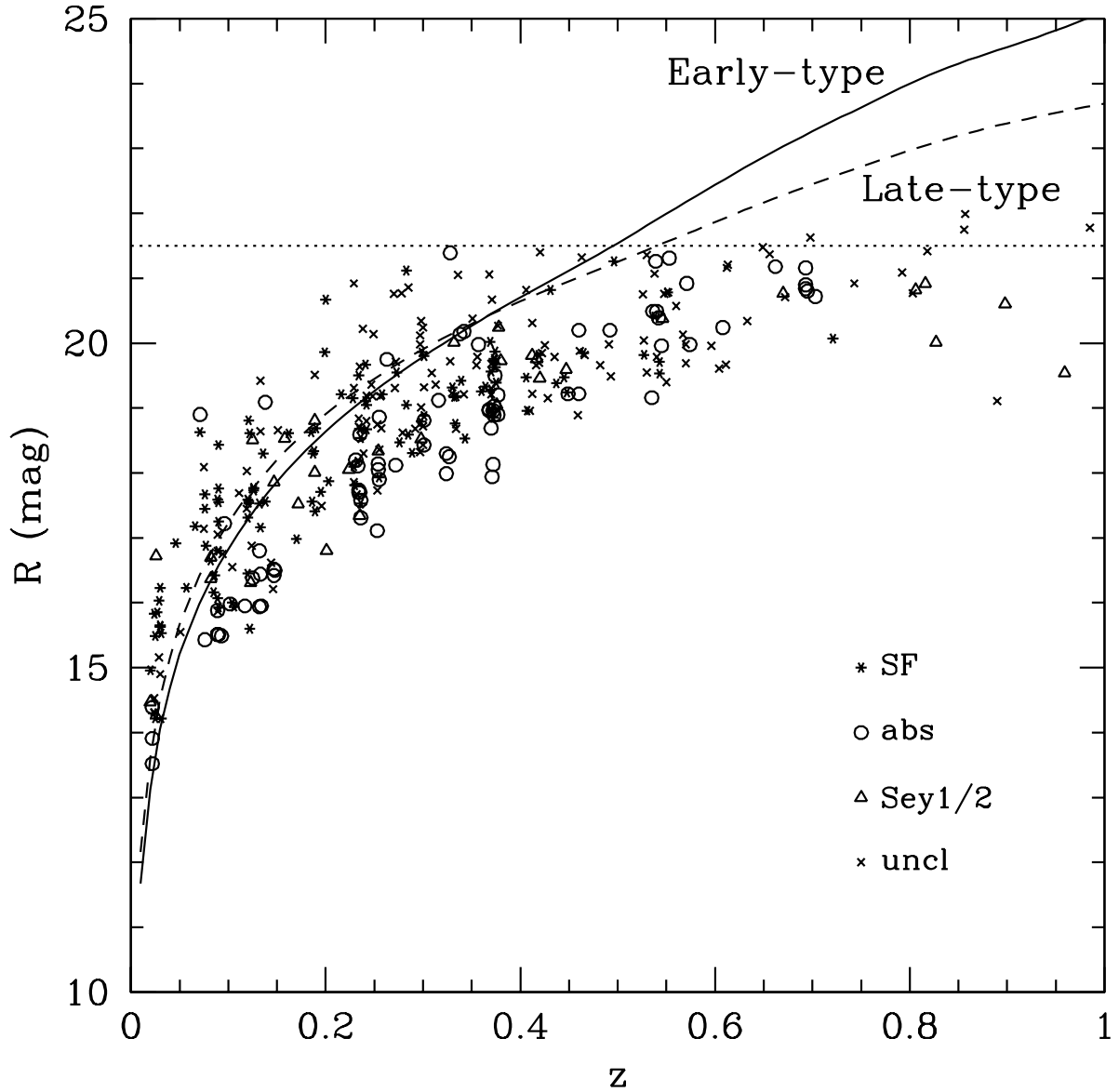


Fig. 4.— R -band magnitude vs. redshift for the sources shown in Figure 3, according to spectral type. The solid and dashed lines represent, respectively, the predicted variation of apparent magnitudes for M^* early- and late-type galaxies, according to the evolutionary scenario of Pozzetti, Bruzual, & Zamorani (1996). The dotted line shows the $R = 21.5$ mag level, indicative of the spectroscopic target selection magnitude limit.

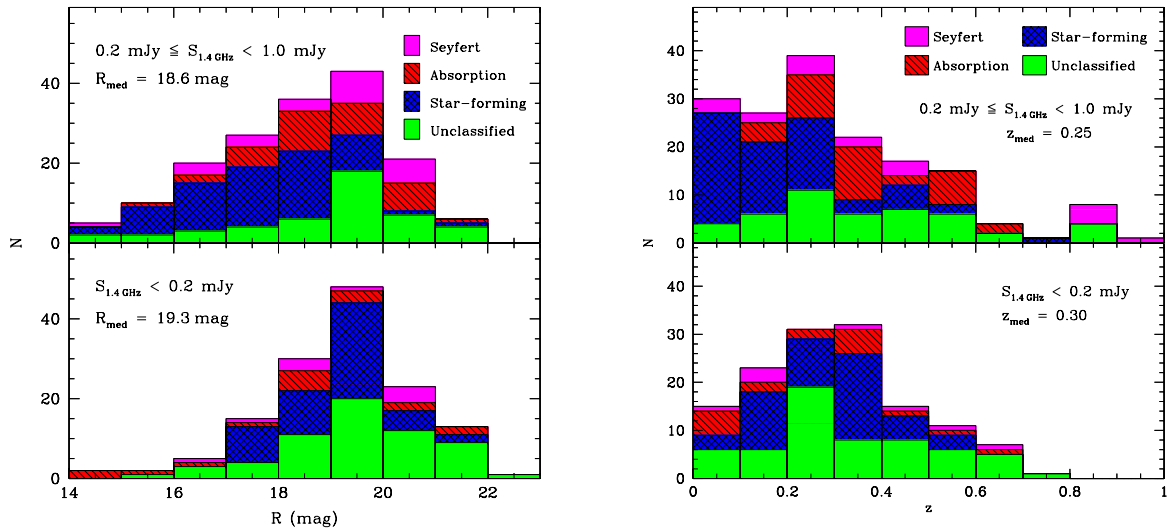


Fig. 5.— Magnitude (left) and redshift (right) distribution for different types of faint radio sources with redshift determination in selected ranges of 1.4 GHz flux density. The median magnitude and redshift for each radio flux interval is indicated.

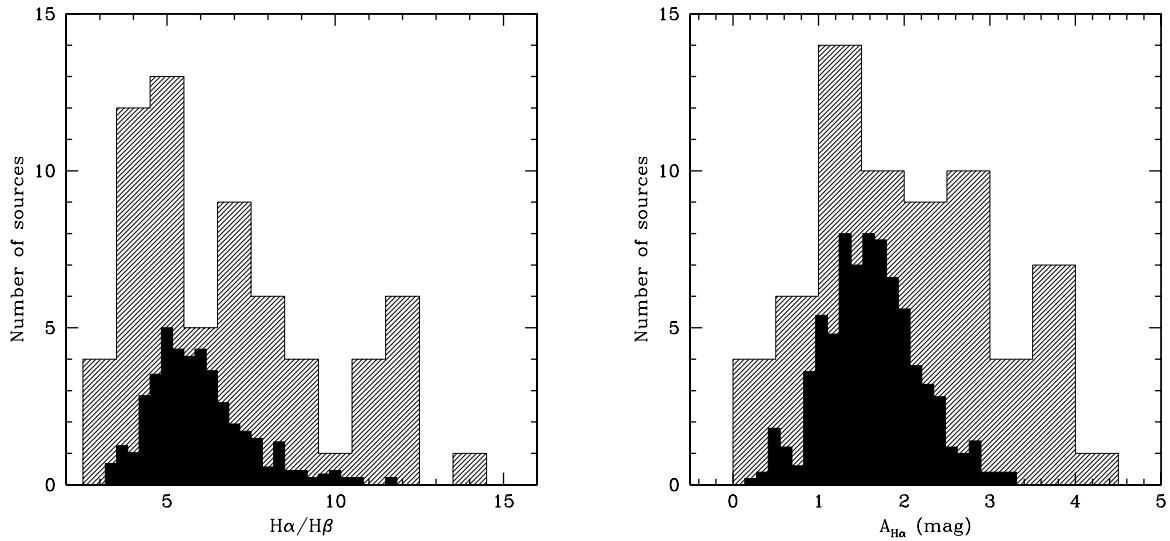


Fig. 6.— Distribution of Balmer decrements (corrected for stellar absorption) of star-forming galaxies in the present sample (left) and derived (emission-line) obscuration values at the $H\alpha$ wavelength for the same galaxies (right). The solid histograms represent the (scaled down) distributions found by Hopkins et al. (2003b) for radio-detected SDSS star-forming galaxies. See text for details.

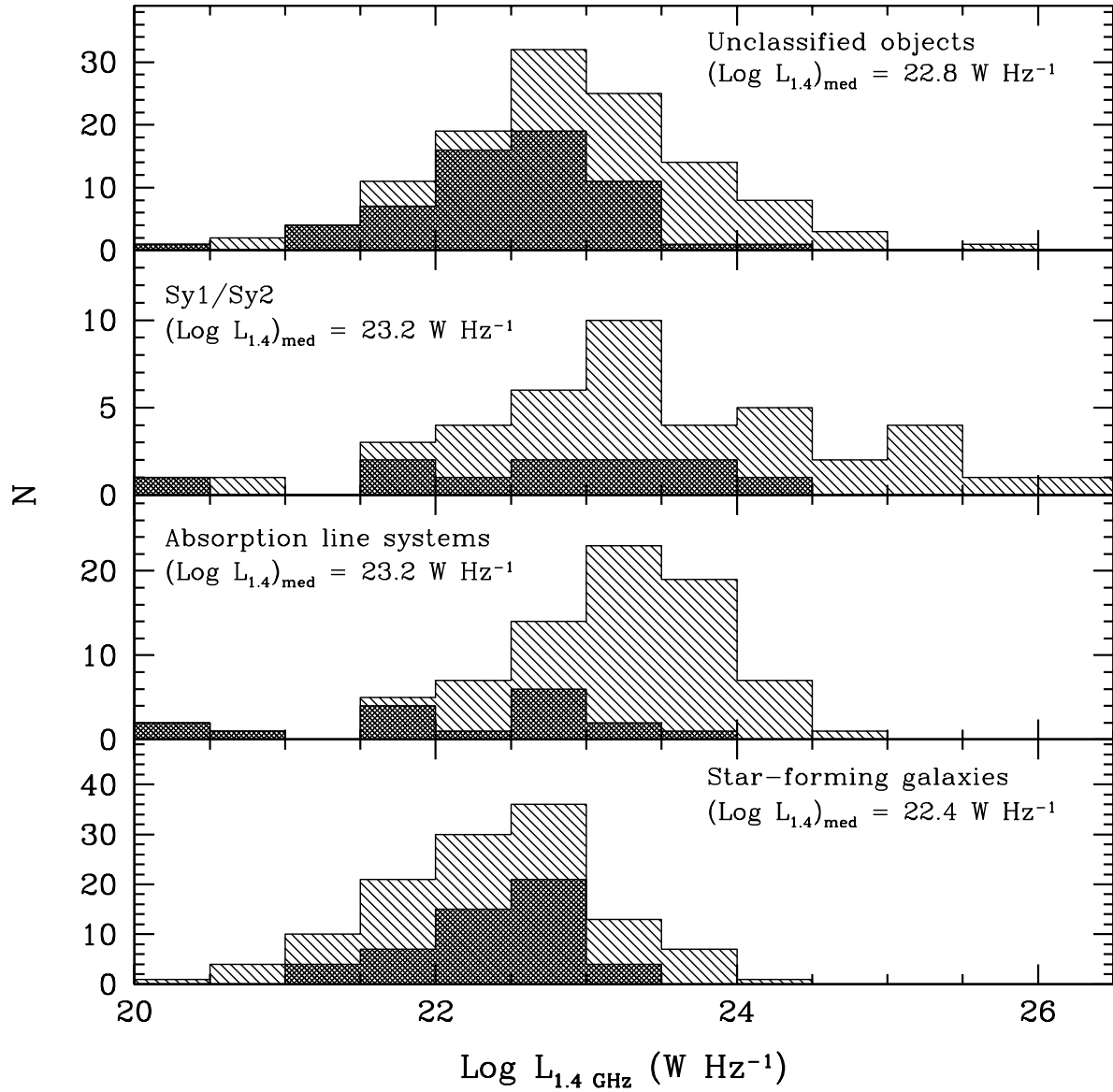


Fig. 7.— Radio luminosity distribution of sub-mJy radio sources according to their spectroscopic classification. The median radio luminosity value is indicated for each class. Sources with 1.4 GHz flux densities below 200 μ Jy are also represented (dark cross-hatched histogram).

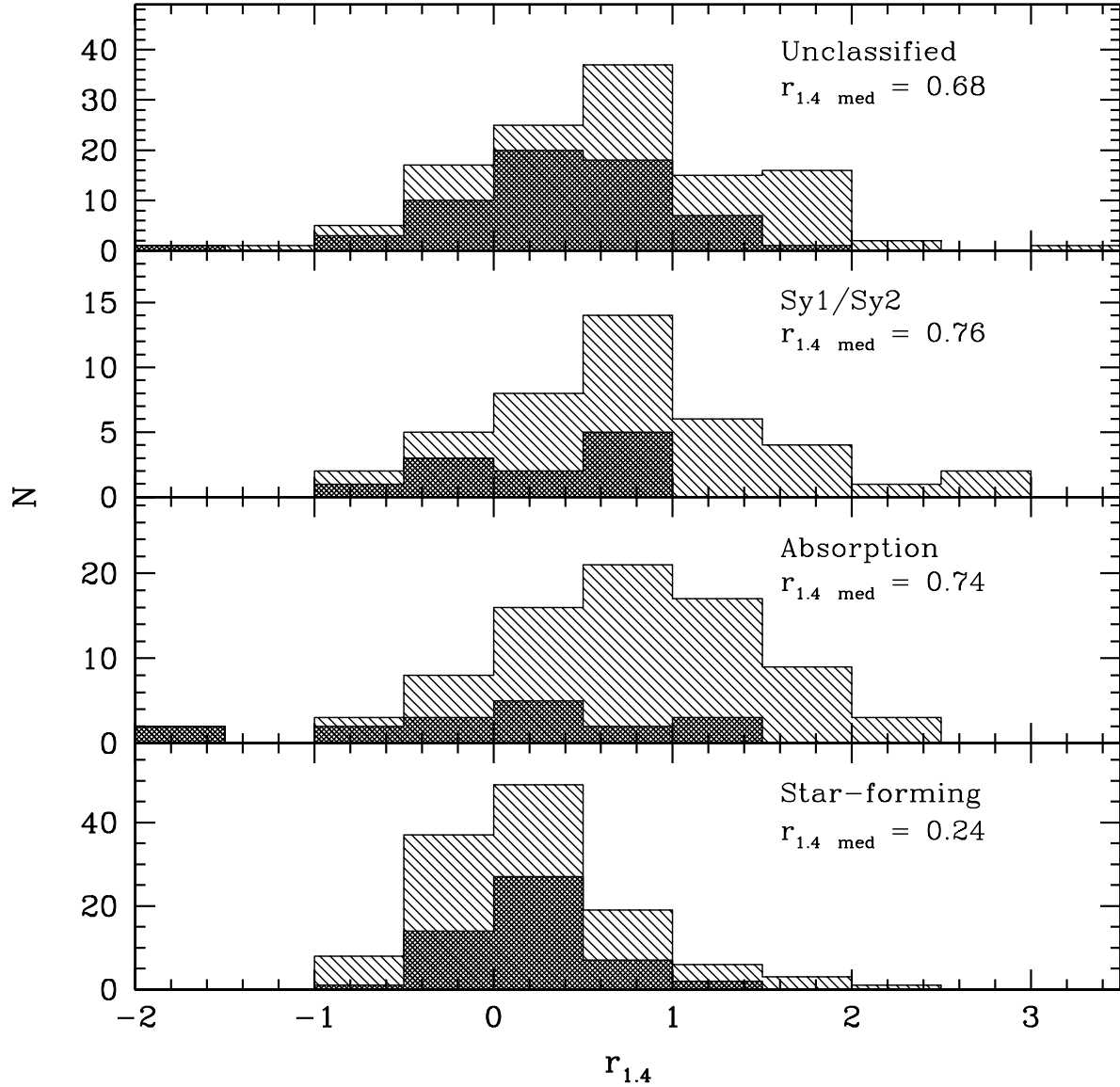


Fig. 8.— Radio-optical flux ratio distribution of sub-mJy radio sources, according to their spectroscopic classification. The median radio-optical flux ratio value is indicated for each class. The dark cross-hatched histogram represents sources with 1.4 GHz flux densities below 200 μJy .

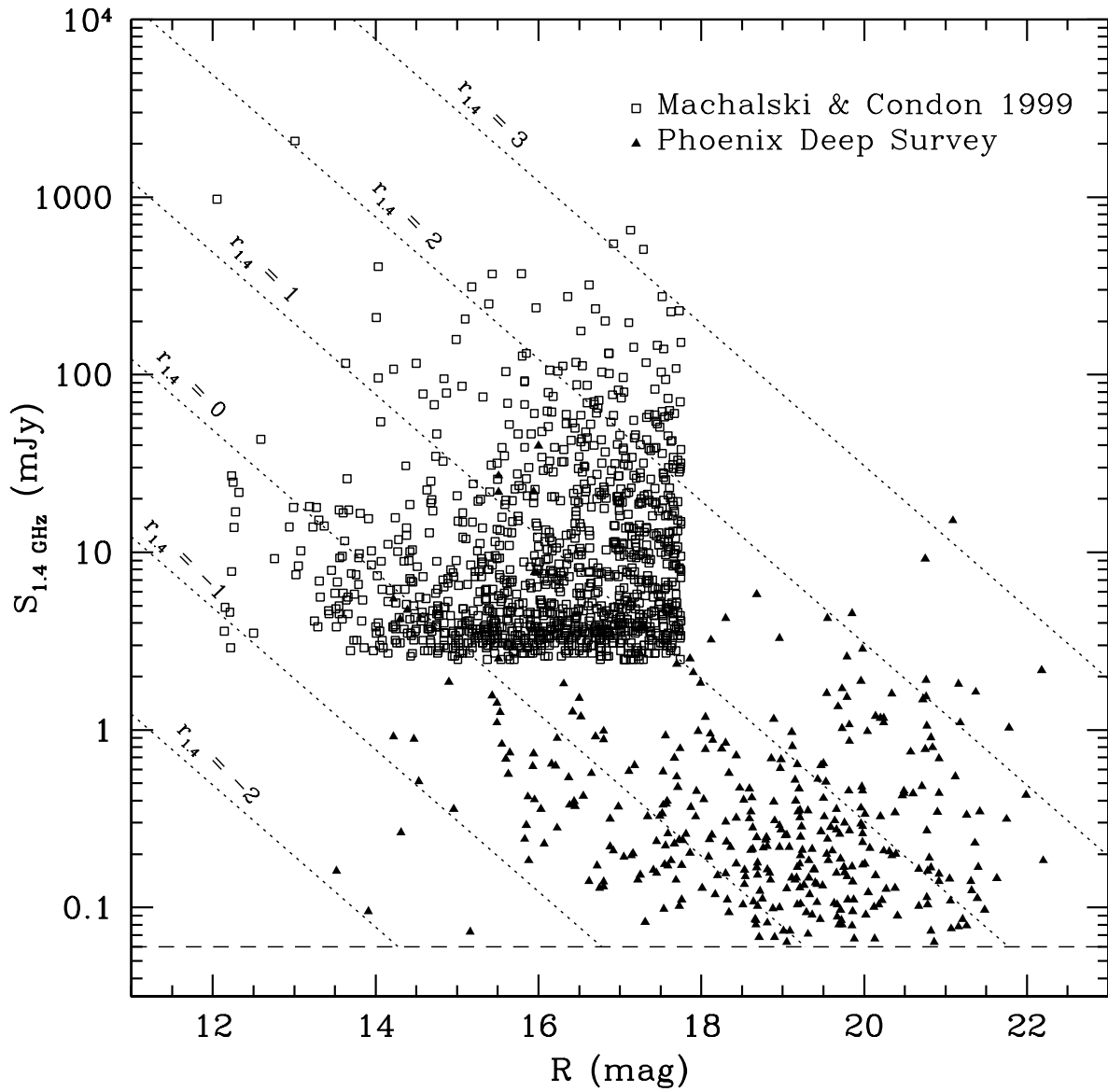


Fig. 9.— Radio-optical flux ratio parameter space covered by the study of Machalski & Condon (1999, open squares) and the sub-mJy sources described here (filled triangles). Diagonal lines show the locus of different values for the $r_{1.4}$ parameter, as indicated, while the dashed horizontal line shows the radio 1.4 GHz flux density limit of the Phoenix sample.

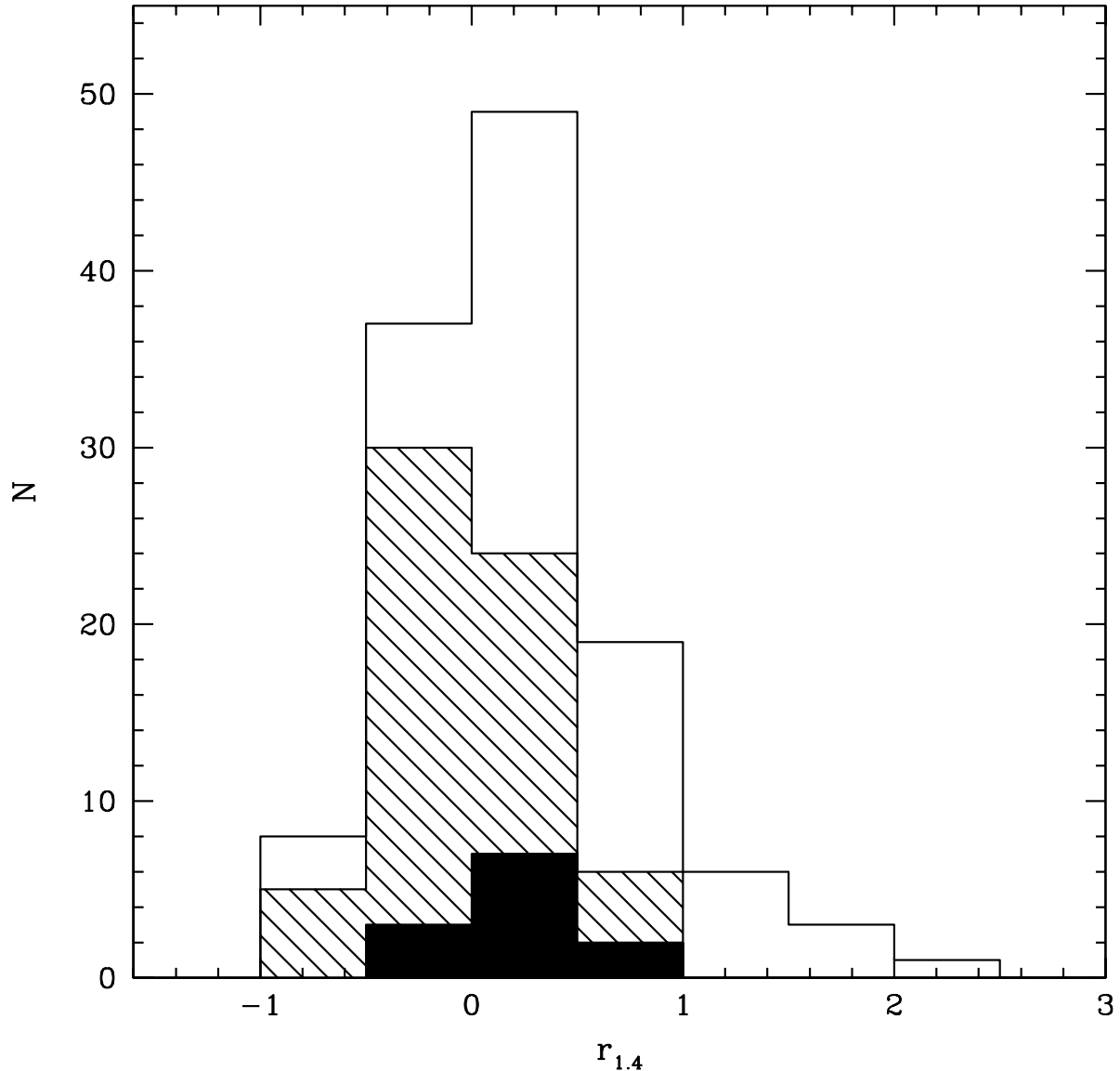


Fig. 10.— Distribution of radio-optical flux ratio for star-forming galaxies. Galaxies with a (Balmer decrement) obscuration measurement are identified (hatched histogram) and, among these, those with the highest obscuration measurements, $A_{H\alpha} > 3$ mag (solid histogram).

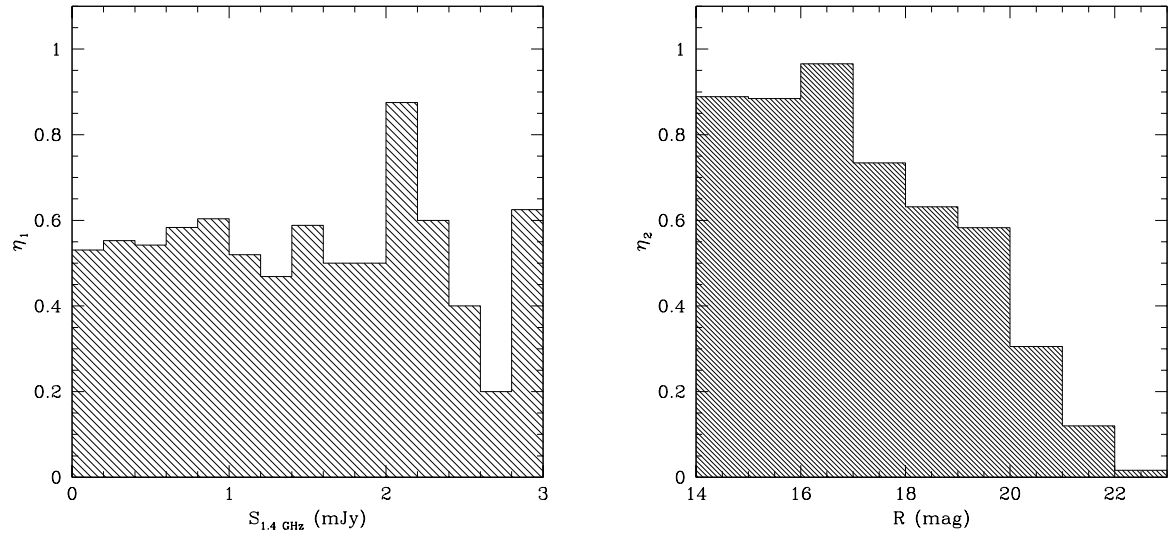


Fig. 11.— Completeness functions used to correct for incompleteness in the determination of the 1.4 GHz luminosity function for star-forming galaxies in the PDS. $\eta_1(S_{1.4 \text{ GHz}})$ is the ratio of the number of radio sources with optical identification to the total number of radio sources within the survey area considered. $\eta_2(R)$ represents the ratio of the number of galaxies with a measured redshift to the total number of sources with optical counterparts in the same sample. Each identified star-forming galaxy contributes to the 1.4 GHz luminosity function correcting for the incompleteness given by $\eta_1(S_{1.4 \text{ GHz}})$ and $\eta_2(R)$ at that galaxy’s radio flux density and R -band magnitude.

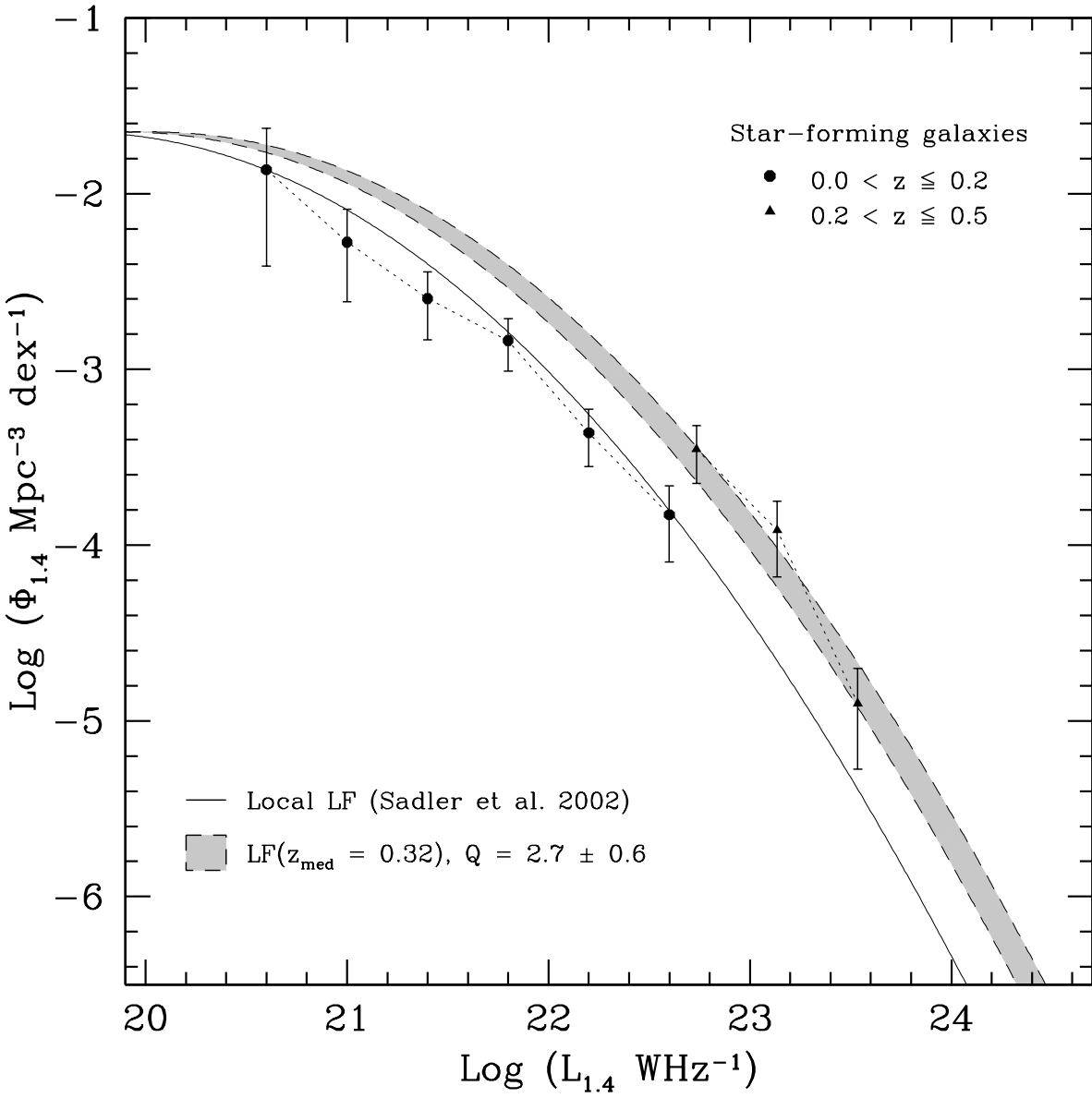


Fig. 12.— Radio (1.4 GHz) luminosity function for star-forming galaxies in the PDS, locally ($z \leq 0.2$, dots) and at intermediate redshifts ($0.2 < z \leq 0.5$, triangles). The parametric fit form for the luminosity function derived by Sadler et al. (2002) is also shown, both in its derived form for local galaxies (solid line) and after applying a simple luminosity evolution in the form $L_{1.4 \text{ GHz}} \propto (1+z)^Q$, with $Q = 2.7 \pm 0.6$ as derived by Hopkins (2004) (shaded region).